INTERNATIONAL JOURNAL OF FLUID MECHANICS RESEARCH
(An Official Journal of the American Society of Thermal and Fluids Engineers)

ISSN Print: 1064-2277
ISSN Online: 2152-5102

PUBLISHER: *BEGELL HOUSE, CONNECTICUT, USA.*

Accepted December 30th 2017

FINITE ELEMENT ANALYSIS OF ROTATING OSCILLATORY MAGNETO-CONVECTIVE RADIATIVE MICROPOLAR THERMO-SOLUTAL FLOW

MD. Shamshuddin [1*], O. Anwar Bég[2] and **Ali Kadir[3]**

[1*]*Department of Mathematics, Vaagdevi College of Engineering, Warangal, Telangana,* ***India****.*
[2,3]*Aeronautical and Mechanical Engineering, University of Salford, Manchester, England,* ***UK.***

*Corresponding author: *Email: mdshamshuddin@vaagdevieng.ac.in*

ABSTRACT

Micropolar fluids provide an alternative mechanism for simulating micro-scale and molecular fluid mechanics which require less computational effort. In the present paper, a numerical analysis is conducted for the primary and secondary flow characterizing dissipative micropolar convective heat and mass transfer from a rotating vertical plate with oscillatory plate velocity, adjacent to a permeable medium. Owing to high temperature, thermal radiation effects are also studied. The micropolar fluid is also chemically-reacting, both thermal and species (concentration) buoyancy effects and heat source/sink are included. The entire system rotates with uniform angular velocity about an axis normal to the plate. Rosseland's diffusion approximation is used to describe the radiative heat flux in the energy equation. The partial differential equations governing the flow problem are rendered dimensionless with appropriate transformation variables. A Galerkin finite element method is employed to solve the emerging multi-physical components of fluid dynamics problem are examined for a variety of parameters including rotation parameter, radiation-conduction parameter, micropolar coupling parameter, Eckert number (dissipation), reaction parameter, magnetic body force parameter and Schmidt number. A comparison with previously published article is made to check the validity and accuracy of the present finite element solutions under some limiting case and excellent agreement is attained. The current simulations may be applicable to various chemical engineering systems, oscillating rheometry, and rotating MHD energy generator near-wall flows.

Keywords: *Thermal radiation, viscous dissipation, oscillation, secondary flow, micropolar fluid, Galerkin finite element method.*

Nomenclature

B_0	applied magnetic field strenth
C	concentration of the solute (*mol* m^{-3})
C_{fx}	primary skin friction coeffcient
C_{fy}	secondary skin friction coeffcient
C_{wx}	primary wall couple stress
C_{wy}	secondary wall couple stress
C_p	specific heat at constant pressure *(J* Kg^{-1} K^{-1}*)*
C_w	concentration of the solute at the plate (*mol* m^{-3})
C_∞	free stream concentration (*mol* m^{-3})
D_m	molecular diffusivity (m^2/s)
Ec	Eckert number
F	Radiation-conduction parameter
Gm	species Grashof number
Gr	thermal Grashof number
j^*	micro inertia per unit mass
K	permeability of porous medium(m^2)
Kr	chemical reaction parameter
M	magnetic field parameter
n	non-dimensionaloscillation frequency
Nu	Nusselt number
Pr	Prandtl number
q_r	Thermal radiative heat flux (W/m^2)
Q	heat source parameter
R	rotational parameter
Re_x	local Reynolds number
S	suction parameter
Sc	Schmidt number
Sh_x	Sherwood number
t	non-dimensional time
T	Temperature of the field (K)
T_w	Wall temperature of the fluid (K)
T_∞	Temperature of the fluid in free stream (K)
u	primary velocity (m)
v	secondary velocity (m)
U_r	uniform reference velocity
$w_1, w_2, w_3, w_4, w_5, w_6$	arbitrary test functions

Greek letters

Δ	Eringen coupling number
β_T	coefficient of thermal expansion (K^{-1})
β_C	coefficient of concentration expansion (K^{-1})
ρ	density of magneto-micropolar fluid($Kg\ m^{-3}$)
σ	electrical conductivity of the fluid ($S\ m^{-1}$)
κ	thermal conductivity ($W\ m^{-1}K^{-1}$)
ν	Kinematic viscosity (m^2/s)
ν_r	Kinematic vortex viscosity (m^2/s)
γ	gyroscopic viscosity (Kg m/s)
λ	Coefficient of gyro-viscosity (Kg m/s)
μ	Fluid dynamic viscosity (Pa s)
θ	Dimensionless temperature
ϕ	Dimensionless concentration
ω_1	primary angular velocity
ω_2	Secondary angular velocity
ψ	shape function

constants

g^*	acceleration due to gravity (m/s)
p	constant pressure
σ^*	Stefan-Boltzmann constant ($W\ m^{-3}\ K^{-4}$)
k^*	mean absorption coefficient(m^{-1})
Ω	constant uniform angular velocity
ε	constant

1. INTRODUCTION

Rotating thermal convection flows arise in an extensive range of industrial systems including rotating heat exchangers, multi-stage cyclone separators, mixing devices in chemical engineering and spin-stabilization of spacecraft vehicles. Rotating fluid systems generate both real and fictitious forces, the former is the centrifugal force and the latter is the Coriolis force. Should the rate of rotation of a body change then a third fictitious force, the Euler force may also be invoked. The interplay between Coriolis force and viscous force have profound effects on for example external boundary layer growth, thermal boundary layer thickness etc. The Coriolis force induces motion in the secondary flow direction. Further complexities arise when the fluid is electrically conducting and when mass transfer (species diffusion) is present. Investigations of boundary layer flows from rotating bodies have included a variety of configurations e.g. rotating plate (Tokis, 1988), spinning sphere (Bég *et al.,* 2015), rotating disk (Kendoush, 2013), rotating cone (Bég *et al.,* 2016) and rotating ellipsoid (Riley, 1996). These studies have shown significant modification in momentum, heat and also mass transfer rates induced by rotational body force. They have however generally been confined to Newtonian fluids. Many non-Newtonian fluids arise in technological applications including polymers, slurries, gels, dusty suspensions etc. They are characterized by complex micro-structure and observations have revealed that such fluids generally deviate from the classical Navier-Stokes viscous flow model. This model cannot simulate the effects of molecular spin since it neglects couple stresses in the constitutive formulation. To address this issue Eringen proposed the *micro-morphic theory of fluids* over five decades ago, of which several special cases have sustained significant interest in engineering sciences. These are the micro-stretch fluid and the micropolar fluid (Eringen, 2001). The latter has received wide attention in heat and mass transfer modelling. The Eringen micropolar theory features additional degrees of freedom (gyratory motions) which allow the physical representation of the rotation of the microstructure. Hence, the balance law of angular momentum is introduced for solving gyration, extending the conventional linear momentum balance in Newtonian models. Molecular spin can therefore be analysed robustly within the framework of micropolar fluid mechanics. An additional advantage is that micropolar models do not require computationally intensive simulations which are necessary for alternative approaches in micro scale fluid dynamics (e.g. Molecular Dynamics, Monte Carlo simulation etc.). Micropolar fluids do not sustain a simple shearing motion, where only one component of velocity is present. In the context of rotating flows, they provide both an assessment of the micro-scale rotary motions and the influence of micro-structural characteristics on global rotational motions. The interest in the present novel investigation arises from a desire to elaborate the collective influence of primary and secondary flow from a spinning rigid body (plate) when the boundaries are subjected to slow rotation. Motivated by geophysical and petrochemical engineering systems, early studies of micropolar transport phenomena from rotating bodies were presented by (Rao *et al*., 1969; Ramkissoon, 1977; Kirwan and Chang, 1976; Sastry and Rao, 1979). These investigations were however confined to fluid flow showing that the presence of micropolar elements enhances momentum boundary layer thickness. One of the earliest comprehensive analyses of micropolar thermal convection from a spinning body was conducted by (Gorla and Takhar, 1994) who also considered heat generation effects. They showed numerically that the momentum, angular momentum (gyration) and thermal boundary layers grow with centrifugal forces. (Gorla, 1995) subsequently analyzed the non-similar mixed convection of a micropolar fluid from a rotating cone, exploring the influence of microrotation boundary conditions on velocity, micro-rotationand heat transfer distributions. The rotationally symmetric flow of micropolar fluids from a rotating

disk was studied by (Nazir *et al.,* 2015) using the successive over relaxation (SOR) method. Very recently (Gajjela *et al.,* 2016) derived analytical solutions for Bejan number in magnetized micropolar rotating annular flow.

These simulations have considered steady-state flows. However, many materials processing systems feature oscillatory flow characteristics induced by periodic motions of the boundary. Periodic flows and judicious selection of oscillation frequency can aid in the diffusion of species and transport of heat. This can be critical in certain flow reactor designs using non-Newtonian liquids (Lee *et al.,* 2001). Many theoretical studies on oscillatory mutli-physical flows have been communicated in recent years. (Bég *et al.,* 2010) derived asymptotic solutions for oscillatory Couette channel hydromagnetic flow with inclined magnetic field and porous medium drag effects. (Reis *et al*., 2004) reported both analytical and experimental results for unsteady oscillatory hydrodynamics in a screening reactor. (Bhargava *et al.*,2009) presented solutions for periodic reactive flow with cross diffusion effects via FEM. (Bég *et al.,* 2012) derived asymptotic solutions for oscillating hydromagnetic flow and heat transfer in couple stress liquids in a spinning bioreactor channel configuration. (Maqbool *et al.,*2016) presented Fourier series solutions for a variety of oscillatory magnetohydrodynamic channel flows, also considering rotational body force and both Newtonian and non-Newtonian material models. Oscillatory micropolar flows in the annular region of two concentric spheres were examined by (Iynger and vani, 2004). Buoyancy effects on magnetic oscillatory flow of micropolar fluids as well as nanofluids were reported by (Kim and Lee, 2003; Modather *et al.,* 2009; Shamshuddin et al., 2017; Thirupathi et al., 2017). (Satya Narayana et al., 2013) reported analytical solutions on oscillatory micropolar flow in rotating system. (Shamshuddin and Thirupathi, 2017) computed cross-diffusion effects on transient dissipative micropolar free convection flows using a finite element technique.

In many materials synthesis operations and in chemical processing, chemical reactions play a significant role. They often occur with mass transfer phenomena. Examples include heterogeneous fluid-solid non-catalytic reactions in metallic processing (Shon, 2003), wall-reactive flows in finishing (coating) of aerospace components (Tischer *et al.,* 2010), chemical vapour deposition systems (Wei *et al.,* 2007) and surface modification of polymers (Kee et al., 2003). The field of chemical reaction fluid mechanics is vast. In the context of boundary layer flows, simple homogenous or heterogeneous chemical reaction models are used. These may be constructive or destructive. In the present study a *homogenous chemical reaction model* is employed. This assumes that the reaction rate depends on the concentration of the species and via a power-law index a range of different reaction orders can be examined. The general n^{th} order reaction rate assumes that chemical reaction rate varies with the n^{th} power of the species concentration. A popular model in mathematical studies is the first order model for which the chemical reaction is directly proportional to the concentration. Many different computational methods have been employed to study reactive heat and mass transfer flows. These include lattice Monte Carlo techniques (Fiedler *et al.,* 2015), finite element methods (Uddin *et al.,* 2015) and finite volume codes (e.g. ANSYS Fluent) (Gomez et al., 2013). Micropolar reactive flows have also been addressed by a number of researchers using both analytical and numerical approaches. (Bakr, 2011) presented closed-form solutions for reactive magnetized rotating natural convective heat and mass diffusion from an oscillating plate in a micropolar fluid. (Abbas *et al*.,2016) obtained shooting quadrature computational solutions for reactive micropolar viscoelastic flow from an extending/contracting sheet in a permeable regime. (Zueco *et al.,*2009) used a n^{th} order reaction

model to investigate two-dimensional micropolar flow and mass transfer in porous media with the network electro-thermal code, PSPICE. (Rahman and Al-Lawatia, 2010) studied reactive boundary layer flow of a micropolar fluid from a non-linear stretching porous sheet in a permeable medium. (Mishra *et al.*,2016) presented numerical solutions for thermos-diffusive and reactive effects on magnetic micropolar convection flows and (Mishra and Bhatti, 2017) also presented numerical solutions on simultaneous effects of chemical reaction and Ohmic heating. Few reactive models including (Satya Narayana et al., 2013; Venkateswarlu and Satya Narayana, 2015)

The above studies generally neglected *thermal radiative heat transfer*. At high temperatures, radiation is the dominant mode of heat transfer. It therefore is intrinsic to many modern manufacturing processes including glass synthesis, coating deposition, chemical reactor vapour deposition, combustion and flame treatment of materials. Radiative heat transfer is also the most complex mode of thermal transport. It involves many complex features including spectral effects, optical thickness, reflection, absorption, transmission etc. To simulate radiative heat transfer problems, very sophisticated numerical algorithms must be employed to cater for a multitude of thermo-physical phenomena which is both time-consuming and expensive. Many approaches have been developed to overcome this challenge and popular models emerging in engineering sciences include the Milne-Eddington approximation, Chandrasekhar discrete ordinates method, P1 differential approximation, Schuster-Schwartzchild two-flux model and the Rosseland diffusion model (Modest, 1992). These methods convert the integro-differential radiative equation into either partial differential equations or algebraic flux equations which are much easier to implement. Many simulations have been presented using these radiative models including (Malpica *et al.*,2003; Mohamed *et al.*, 2003; Pai and Scaglione, 1970; Murthy *et al.*, 2017; Bhatti *et al.*, 2017; Pal and Talukdar, 2012; Olajuwon and Oahimire, 2013; Bakr, 2013; Swapna *et al.*, 2015; Seth *et al.*, 2011; Das, 2011; Harish Babu and Satya Narayana 2013; Satya Narayana et al., 2015).

In the present article, we investigate the buoyancy-driven primary and secondary flow with heat and mass transfer in a rotating electrically-conducting reactive micropolar fluid adjacent to an oscillating vertical plate in a porous medium under substantial thermal radiation. The Darcy model is utilized (Bég *et al.*, 2016) and the Rosseland radiative flux model adopted. Viscous dissipation is also considered as it has been shown to contribute significantly in micropolar flows (Khonsari and Brewe, 1994). Although the current study is theoretical, the physical justification for the micropolar model has been documented by (Papautsky *et al.*,1999). Numerical solutions are developed using the versatile Galerkin finite element technique. As such we generalize the previous analytical (perturbation) solutions of (Bakr, 2011; Bakr, 2013) to consider combined Rosseland flux and porous media effects, simultaneously validating the present finite element code**.** The current study is relevant to *reactive magnetic non-Newtonian materials processing* and certain *magnetohydrodynamic (MHD) energy generator* configurations featuring rotating components (Rosa, 1987).

2. MATHEMATICAL FORMULATION OF THE PROBLEM

The case of unsteady natural convective flow, heat and mass transfer of an electrically conducting incompressible micro-polar fluid from a vertical plane in an isotropic saturated porous medium is considered. The plate and fluid like in the x^*-z^* plane and both are rotating in unison with constant

uniform angular velocity Ω about the z^*-axis with a velocity $u^* = U_r\left(1+\varepsilon \cos n^* t^*\right)$.Initially at time $t^* \le 0$ both the plate and fluid are at rest and are maintained at a uniform temperature T_∞^* and concentration C_∞^*. At time $t^* > 0$, the plate starts moving in the *x**-direction with uniform velocity U_r in its own plane, thereafter the plate is maintained at constant temperature T_w^* and concentration C_w^*. These values are assumed to be greater than the ambient temperature T_∞^* and concentration C_∞^* .The physical configuration is illustrated in **Fig. 1.**

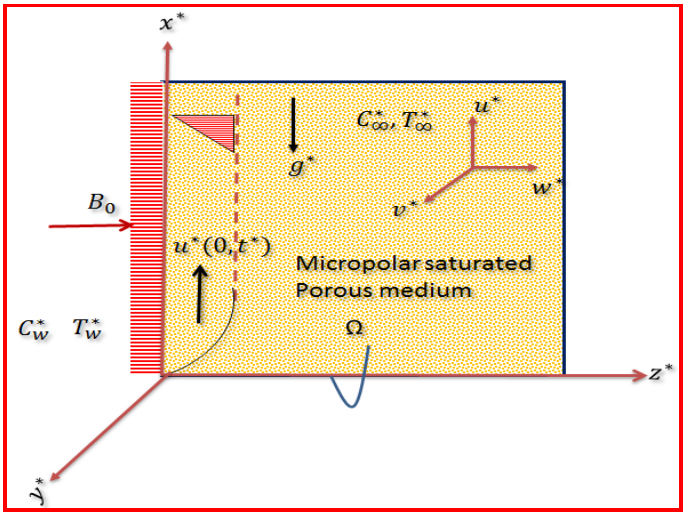

FIG. 1. Geometry and coordinate system

A uniform magnetic field of strength B_0 is applied normal to the flow direction. It is assumed that the induced magnetic field is negligible in comparison to the applied magnetic field (Malpica *et al.*, 2003). Since the magnetic Reynolds number of the flow is taken to be very small, the induced magnetic field is neglected so that magnetic field $B = (0,\ Bo,\ 0)$. It is also assumed that no external electric field is applied so the electric field due to polarization of charges is negligible (Seth et al., 2013; Satya Narayana et al., 2013) ($E = (0,\ 0,\ 0)$)which corresponds that applied or polarized voltage is neglected so that no energy is added or extracted from the fluid by electrical means. Ohmic (Joule) heating is neglected as are Soret and Dufour cross-diffusion effects. The first order species concentration has also been incorporated in the mass transfer equation.
The Boussinesq approximation is taken and invokes thermal and species buoyancy body forces in the primary momentum equation, as follows:

$$\frac{\partial w^*}{\partial z^*} = 0 \tag{1}$$

$$\frac{\partial u^*}{\partial t^*} + w^* \frac{\partial u^*}{\partial z^*} - 2\Omega v^* = \left(\nu + \nu_r\right)\frac{\partial^2 u^*}{\partial z^{*2}} + g^* \beta_T \left(T^* - T_\infty^*\right) + g^* \beta_C \left(C^* - C_\infty^*\right) - \frac{\sigma B_0^2 u^*}{\rho} - \frac{\nu u^*}{k} - \nu_r \frac{\partial \bar{\omega}_2^*}{\partial z^*} \tag{2}$$

$$\frac{\partial v^*}{\partial t^*} + w^* \frac{\partial v^*}{\partial z^*} + 2\Omega u^* = \left(\nu + \nu_r\right)\frac{\partial^2 v^*}{\partial {z^*}^2} - \frac{\sigma B_0^2 v^*}{\rho} - \frac{\nu w^*}{k} + \nu_r \frac{\partial \overline{\omega}_1^*}{\partial z^*} \tag{3}$$

$$\frac{\partial \overline{\omega}_1^*}{\partial t^*} + w^* \frac{\partial \overline{\omega}_1^*}{\partial z^*} = \frac{\gamma}{\rho j^*}\frac{\partial^2 \overline{\omega}_1^*}{\partial {z^*}^2} \tag{4}$$

$$\frac{\partial \overline{\omega}_2^*}{\partial t^*} + w^* \frac{\partial \overline{\omega}_2^*}{\partial z^*} = \frac{\gamma}{\rho j^*}\frac{\partial^2 \overline{\omega}_2^*}{\partial {z^*}^2} \tag{5}$$

$$\frac{\partial T}{\partial t^*} + w^* \frac{\partial T}{\partial z^*} = \frac{\kappa}{\rho C_p}\frac{\partial^2 T}{\partial {y^*}^2} - \frac{1}{\rho C_p}\frac{\partial q_r}{\partial z^*} - \frac{Q^*}{\rho C_p}\left(T^* - T_\infty^*\right) + \frac{\mu}{\rho C_p}\left(\frac{\partial u^*}{\partial z^*}\right)^2 \tag{6}$$

$$\frac{\partial C}{\partial t^*} + w^* \frac{\partial C}{\partial z^*} = D_m \frac{\partial^2 C}{\partial {z^*}^2} - K'r\left(C^* - C_\infty^*\right) \tag{7}$$

Here u^*, v^* and w^* are velocity components along x^*, y^* and z^*-axis respectively, $\overline{\omega}_1$ and $\overline{\omega}_2$ are angular velocity components along the x^* and y^* directions respectively,

The relevant and appropriate initial and boundary conditions are given by:

$$\left.\begin{array}{l} t^* \le 0 : \left\{ u^* = v^* = 0, \quad \overline{\omega}_1^* = \overline{\omega}_2^* = 0, T^* = T_\infty^*, C^* = C_\infty^*. \right. \\ t^* > 0 : \left\{ \begin{array}{ll} u^* = U_r\left[1 + \frac{\varepsilon}{2}\left(e^{in^*t^*} + e^{-in^*t^*}\right)\right], v^* = 0, \overline{\omega}_1^* = -\frac{1}{2}\frac{\partial v^*}{\partial z^*}, \overline{\omega}_2^* = \frac{1}{2}\frac{\partial u^*}{\partial z^*}, T^* = T_w, C^* = C_w & at\ z^* = 0 \\ u^* \to 0, v^* \to 0, \quad \overline{\omega}_1^* \to 0, \overline{\omega}_2^* \to 0, T^* \to T_\infty^*, C^* \to C_\infty^* & as\ z^* \to \infty \end{array} \right. \end{array}\right\} \tag{8}$$

The oscillatory plate velocity assumed in Eq. (8) is based on the model proposed by (Ganapathy, 1994). Integrating the continuity equation (1) for variable transpiration (lateral mass flux) velocity normal to the plate, a convenient solution emerges as:

$$w^* = -w_0 \tag{9}$$

Here w_0 is the normal velocity at the plate $w_0 > 0$ for suction, $w_0 < 0$ for blowing, while $w_0 = 0$ corresponds to an impermeable plate. The radiative heat flux expression in Eq. (6) is given by Rosseland approximation (Modest, 1992) as

$$q_r = \frac{-4\sigma^*}{3k^*}\left(\frac{\partial {T^*}^4}{\partial z^*}\right) \tag{10}$$

Using Taylor's series expansion about T_∞^* the expansion of ${T^*}^4$ can be written as follows, neglecting higher order terms: (Raptis and Perdikis, 1998)

$${T^*}^4 = {T_\infty^*}^4 + 4{T_\infty^*}^3\left(T^* - T_\infty^*\right) + 6{T_\infty^*}^2\left(T^* - T_\infty^*\right)^2 + \ldots\ldots\ldots\ldots\ldots \tag{11}$$

Neglecting higher order terms beyond the first degree in $\left(T^* - T_\infty^*\right)$, we have

$${T^*}^4 \cong 4T_\infty^{*3}T - 3T_\infty^{*4} \tag{12}$$

Now differentiating (10) w.r.t. the coordinate z^* and invoking eqn. (11), we get:

$$\frac{\partial q_r}{\partial z^*} = -\left(\frac{16\sigma^*}{3k^*}\right) T_\infty^3 \frac{\partial^2 T}{\partial z^{*2}} \tag{13}$$

Substituting T^3 in Eqn. (10) with T_∞^3, Eqn. (6) can then be expressed as follows:

$$\rho C_p \left(\frac{\partial T}{\partial t^*} + w^* \frac{\partial T}{\partial z^*}\right) = \left(\kappa + \frac{16\sigma^*}{3k^*} T_\infty^3\right) \frac{\partial^2 T}{\partial z^{*2}} - Q^* \left(T^* - T_\infty^*\right) + \mu \left(\frac{\partial u^*}{\partial z^*}\right)^2 \tag{14}$$

It is pertinent to note that if this assumption is neglected, the radiative heat flux in Eqn. (6) results in a highly non-linear expression. In that case the energy equation for non-linear thermal radiation with augmented thermal conductivity becomes:

$$\rho C_p \left(\frac{\partial T}{\partial t^*} + w^* \frac{\partial T}{\partial z^*}\right) = \frac{\partial}{\partial z^*}\left[\left(\kappa + \frac{16\sigma^*}{3k^*} T_\infty^3\right) \frac{\partial T}{\partial z^*}\right] - Q^* \left(T^* - T_\infty^*\right) + \mu \left(\frac{\partial u^*}{\partial z^*}\right)^2 \tag{15}$$

Although the primitive conservation equations and boundary conditions (1) -(5), (7), (8) and (14) can be solved with a variety of numerical methods e.g. Crank-Nicolson difference scheme, their solution requires explicit data for thermo-physical properties. It is therefore judicious to render the system dimensionless. The following non-dimensional variables are introduced therefore:

$$\left.\begin{aligned}
&z = \frac{z^* U_r}{\nu}, u = \frac{u^*}{U_r}, v = \frac{v^*}{U_r}, t = \frac{t^* U_r^2}{\nu}, n = \frac{n^* \nu}{U_r^2}, \omega_1 = \frac{\overline{\omega}_1^* \nu}{U_r^2}, \omega_2 = \frac{\overline{\omega}_2^* \nu}{U_r^2}, \\
&\theta = \frac{T - T_\infty}{T_w - T_\infty}, \ \phi = \frac{C - C_\infty}{C_w - C_\infty}, M = \frac{\sigma B_o^2 \nu}{\rho U_r^2}, \ R = \frac{2\Omega\nu}{U_r^2}, G_r = \frac{\nu g^* \beta_T \left(T_w - T_\infty\right)}{U_r^3}, \\
&G_m = \frac{\nu g^* \beta_C \left(C_w - C_\infty\right)}{U_r^3}, S = \frac{w_0}{U_r}, Pr = \frac{\mu \rho C_p}{\kappa}, Sc = \frac{\nu}{D_m}, \ F = \frac{4T_\infty^3 \sigma^*}{\kappa \kappa^*}, \\
&Q = \frac{Q^* \nu^2}{\kappa U_r^2}, Ec = \frac{U_r^2}{C_p (T_w - T_\infty)}, K = \frac{\kappa U_r^2}{\nu^2}, Kr = \frac{K' r \nu}{U_r}, \Delta = \frac{K}{\rho\nu}, \ \lambda = \frac{\gamma}{\mu j^*} = \left(1 + \frac{\Delta}{2}\right)
\end{aligned}\right\} \tag{16}$$

Quantities with superscript * are dimensionless, *z* is dimensionless coordinate along the plate length. All quantities which are dimensionless mentioned in nomenclature. Assimilating the dimensionless variables (16) into equations (1) -(5), (7) and (14) yields the following system of unsteady dimensionless partial differential equations:

$$\frac{\partial u}{\partial t} - S\frac{\partial u}{\partial z} - Rv = (1+\Delta)\frac{\partial^2 u}{\partial z^2} + Gr\theta + Gm\phi - \left(M + \frac{1}{K}\right)u - \Delta\frac{\partial \omega_2}{\partial z} \tag{17}$$

$$\frac{\partial v}{\partial t} - S\frac{\partial v}{\partial z} + Ru = (1+\Delta)\frac{\partial^2 v}{\partial z^2} - \left(M + \frac{1}{K}\right)v + \Delta\frac{\partial \omega_1}{\partial z} \tag{18}$$

$$\frac{\partial \omega_1}{\partial t} - S\frac{\partial \omega_1}{\partial z} = \lambda\frac{\partial^2 \omega_1}{\partial z^2} \tag{19}$$

$$\frac{\partial \omega_2}{\partial t} - S\frac{\partial \omega_2}{\partial z} = \lambda\frac{\partial^2 \omega_2}{\partial z^2} \tag{20}$$

$$\frac{\partial \theta}{\partial t} - S\frac{\partial \theta}{\partial z} = \frac{1}{Pr}\left(1 + \frac{4F}{3}\right)\frac{\partial^2 \theta}{\partial z^2} - \frac{Q}{Pr}\theta + Ec\left(\frac{\partial u}{\partial z}\right)^2 \tag{21}$$

$$\frac{\partial \phi}{\partial t} - S\frac{\partial \phi}{\partial z} = \frac{1}{Sc}\frac{\partial^2 \phi}{\partial z^2} - Kr\ \phi \tag{22}$$

Dimensionless initial and boundary conditions are

$$\left.\begin{array}{l} for\ t \le 0: \begin{cases} u = v = 0 \quad \omega_1 = \omega_2 = 0\ \theta = 0, \phi = 0 \end{cases} \\ for\ t > 0: \begin{cases} u = 1 + \dfrac{\varepsilon}{2}\left(e^{int} + e^{-int}\right), v = 0, \omega_1 = -\dfrac{1}{2}\dfrac{\partial v}{\partial z}, \omega_2 = \dfrac{1}{2}\dfrac{\partial u}{\partial z}, \theta = 1, \phi = 1 \quad at\ z = 0 \\ u \to 0, v \to 0, \quad \omega_1 \to 0, \omega_2 \to 0, \quad \theta \to 0, \phi \to 0 \qquad as\ z \to \infty \end{cases} \end{array}\right\} \tag{23}$$

3. GALERKIN FINITE ELEMENT NUMERICAL SOLUTION

3.1 Finite Element Method

The set of partial differential equations (17)-(22) subject to initial and boundary conditions (23) are nonlinear and strongly coupled. The finite element method is therefore adopted to solve this system. FEM remains the most versatile numerical method for engineering sciences. It uses integration rather than differentiation which smooths solutions faster and leads to greater accuracy and faster convergence. The variational form is especially popular for fluid mechanics and transport phenomena simulations and succinct appraisals of this approach are provided by (Reddy, 1985). Although the method has been used in many micropolar fluid mechanics problems, most applications have been steady-state. Recent *unsteady micropolar flow* studies employing FEM include magnetic micropolar nanofluid cavity flow (Turk and Tezer-Sezgin, 2017) and micropolar flow from an oblique surface (Shamshuddin *et al.*, 2017). The five basic fundamental steps can be referred in (Shamshuddin *et al.*, 2017).

3.2 Variational formulation

The variational formulation associated with Eqs. (24) - (29) over a typical two-node linear element $\left(z_e, z_{e+1}\right)$ is given by:

$$\int_{z_e}^{z_{e+1}} w_1\left[\frac{\partial u}{\partial t} - S\frac{\partial u}{\partial z} - Rv - A_1\frac{\partial^2 u}{\partial z^2} - (Gr\theta + Gm\phi) + A_2 u + A_3\frac{\partial \omega_2}{\partial z}\right]dz = 0 \tag{24}$$

$$\int_{z_e}^{z_{e+1}} w_2\left[\frac{\partial v}{\partial t} - S\frac{\partial v}{\partial z} + Ru - A_1\frac{\partial^2 v}{\partial z^2} + A_2 v - A_3\frac{\partial \omega_1}{\partial z}\right]dz = 0 \tag{25}$$

$$\int_{z_e}^{z_{e+1}} w_3\left[\frac{\partial \omega_1}{\partial t} - S\frac{\partial \omega_1}{\partial z} - \lambda\frac{\partial^2 \omega_1}{\partial z^2}\right]dz = 0 \tag{26}$$

$$\int_{z_e}^{z_{e+1}} w_4\left[\frac{\partial \omega_2}{\partial t} - S\frac{\partial \omega_2}{\partial z} - \lambda\frac{\partial^2 \omega_2}{\partial z^2}\right]dz = 0 \tag{27}$$

$$\int_{z_e}^{z_{e+1}} w_5\left[\frac{\partial \theta}{\partial t} - S\frac{\partial \theta}{\partial z} - A_4\frac{\partial^2 \theta}{\partial z^2} + A_5\theta - Ec\left(\frac{\partial u}{\partial z}\right)^2\right]dz = 0 \tag{28}$$

$$\int_{z_e}^{z_{e+1}} w_6\left[\frac{\partial \phi}{\partial t} - S\frac{\partial \phi}{\partial z} - \frac{1}{Sc}\frac{\partial^2 \phi}{\partial z^2} + Kr\ \phi\right]dz = 0 \tag{29}$$

where $A_1 = 1+\Delta,\ A_2 = (M+(1/K))$, $A_3 = \Delta$, $A_4 = (1+(4F/3))/Pr$, $A_5 = (Q/Pr)$. After dropping the order of integration and non-linearity, we arrive at the following system of equations:

$$\int_{z_e}^{z_{e+1}} \left[\begin{array}{l} w_1 \frac{\partial u}{\partial t} - Sw_1 \frac{\partial u}{\partial z} - Rw_1 v + A_1 \frac{\partial w_1}{\partial z}\frac{\partial u}{\partial z} - (Gr\ w_1\theta + Gmw_1\phi) \\ + A_2 w_1 u + A_3 w_1 \frac{\partial \omega_2}{\partial z} \end{array} \right] dz - \left[w_1 \left(\frac{\partial u}{\partial z} \right) \right]_{z_e}^{z_{e+1}} = 0 \quad (30)$$

$$\int_{z_e}^{z_{e+1}} \left[w_2 \frac{\partial u}{\partial t} - Sw_2 \frac{\partial v}{\partial z} + Rw_2 u + A_1 \frac{\partial w_2}{\partial z}\frac{\partial v}{\partial z} + A_2 w_2 v - A_3 w_2 \frac{\partial \omega_1}{\partial z} \right] dz - \left[w_2 \left(\frac{\partial v}{\partial z} \right) \right]_{z_e}^{z_{e+1}} = 0 \quad \textbf{(31)}$$

$$\int_{z_e}^{z_{e+1}} \left[w_3 \frac{\partial \omega_1}{\partial t} - Sw_3 \frac{\partial \omega_1}{\partial z} - \lambda \frac{\partial w_3}{\partial z}\frac{\partial \omega_1}{\partial z} \right] dz - \left[w_3 \left(\frac{\partial \omega_1}{\partial z} \right) \right]_{z_e}^{z_{e+1}} = 0 \quad (32)$$

$$\int_{z_e}^{z_{e+1}} \left[w_4 \frac{\partial \omega_2}{\partial t} - Sw_4 \frac{\partial \omega_2}{\partial z} - \lambda \frac{\partial w_4}{\partial z}\frac{\partial \omega_2}{\partial z} \right] dz - \left[w_4 \left(\frac{\partial \omega_2}{\partial z} \right) \right]_{z_e}^{z_{e+1}} = 0 \quad (33)$$

$$\int_{z_e}^{z_{e+1}} \left[w_5 \frac{\partial \theta}{\partial t} - Sw_5 \frac{\partial \theta}{\partial z} + A_4 \left(\frac{\partial w_5}{\partial z} \right)\left(\frac{\partial \theta}{\partial z} \right) + A_5 w_5 \theta - Ec\ w_5 \left(\frac{\partial \bar{u}}{\partial z} \right)\left(\frac{\partial u}{\partial z} \right) \right] dz - \left[w_5 \left(\frac{\partial \theta}{\partial z} \right) \right]_{z_e}^{z_{e+1}} = 0 \quad (34)$$

$$\int_{z_e}^{z_{e+1}} \left[w_6 \frac{\partial \phi}{\partial t} - Sw_6 \frac{\partial \phi}{\partial z} + \frac{1}{Sc} \frac{\partial w_6}{\partial z}\frac{\partial \phi}{\partial z} + Kr\ w_6\ \phi \right] dz - \left[\frac{w_6}{Sc} \left(\frac{\partial \phi}{\partial z} \right) \right]_{z_e}^{z_{e+1}} = 0 \quad (35)$$

3.3 Finite Element formulation

By substituting finite element approximations of the form in Eqs. (30) - (35), finite element model may be obtained

$$u = \sum_{j=1}^{2} u_j^e \psi_j^e,\ v = \sum_{j=1}^{2} v_j^e \psi_j^e,\ \omega_1 = \sum_{j=1}^{2} \omega_{1j}^e \psi_j^e,\ \omega_2 = \sum_{j=1}^{2} \omega_{2j}^e \psi_j^e,\ \theta = \sum_{j=1}^{2} \theta_j^e \psi_j^e \quad (36)$$

Also ψ_i^e are the shape functions for this element (z_e, z_{e+1})which are defined as:

$$\psi_1^e = \frac{z_{e+1} - z}{z_{e+1} - z_e} and\ \psi_2^e = \frac{z - z_e}{z_{e+1} - z_e},\ z_e \le z \le z_{e+1} \quad (37)$$

The finite element model of the equations for e^{th} element thus formed is given by

$$\begin{bmatrix} [K^{11}] & [K^{12}] & [K^{13}] & [K^{14}] & [K^{15}] & [K^{16}] \\ [K^{21}] & [K^{22}] & [K^{23}] & [K^{24}] & [K^{25}] & [K^{26}] \\ [K^{31}] & [K^{32}] & [K^{33}] & [K^{34}] & [K^{35}] & [K^{36}] \\ [K^{41}] & [K^{42}] & [K^{43}] & [K^{44}] & [K^{45}] & [K^{46}] \\ [K^{51}] & [K^{52}] & [K^{53}] & [K^{54}] & [K^{55}] & [K^{56}] \\ [K^{61}] & [K^{62}] & [K^{63}] & [K^{64}] & [K^{65}] & [K^{66}] \end{bmatrix} \begin{Bmatrix} \{u^e\} \\ \{v^e\} \\ \{\omega_1^e\} \\ \{\omega_2^e\} \\ \{\theta^e\} \\ \{\phi^e\} \end{Bmatrix} + \begin{bmatrix} [M^{11}] & [M^{12}] & [M^{13}] & [M^{14}] & [M^{15}] & [M^{16}] \\ [M^{21}] & [M^{22}] & [M^{23}] & [M^{24}] & [M^{25}] & [M^{26}] \\ [M^{31}] & [M^{32}] & [M^{33}] & [M^{34}] & [M^{35}] & [M^{36}] \\ [M^{41}] & [M^{42}] & [M^{43}] & [M^{44}] & [M^{45}] & [M^{46}] \\ [M^{51}] & [M^{52}] & [M^{53}] & [M^{54}] & [M^{55}] & [M^{56}] \\ [M^{61}] & [M^{62}] & [M^{63}] & [M^{64}] & [M^{65}] & [M^{66}] \end{bmatrix} \begin{Bmatrix} \{u'^e\} \\ \{v'^e\} \\ \{\omega_1'^e\} \\ \{\omega_2'^e\} \\ \{\theta'^e\} \\ \{\psi'^e\} \end{Bmatrix} = \begin{Bmatrix} \{b^{1e}\} \\ \{b^{2e}\} \\ \{b^{3e}\} \\ \{b^{4e}\} \\ \{b^{5e}\} \\ \{b^{6e}\} \end{Bmatrix} \quad (38)$$

Where $\{[K^{mn}], [M^{mn}]\}$ and $\{\{u^e\}, \{v^e\}, \{\omega_1^e\}, \{\omega_2^e\}, \{\theta^e\}, \{\phi^e\}, \{u'^e\}, \{v'^e\}, \{\omega_1'^e\}, \{\omega_2'^e\} \{\theta'^e\}, \{\phi'^e\} and \{b^{me}\}\}$ m, n=1,2,3,4,5,6)denote the set of matrices of order 2×2 and 2×1 respectively and prime $(')$

indicates $\frac{d}{dz}$.

$$\begin{cases} K_{ij}^{11}=-S\int_{z_e}^{z_{e+1}}\left[\left(\psi_i^e\right)\left(\frac{\partial\psi_j^e}{\partial z}\right)\right]dz,\ K_{ij}^{12}=A_1\int_{z_e}^{z_{e+1}}\left[\left(\frac{\partial\psi_i^e}{\partial z}\right)\left(\frac{\partial\psi_j^e}{\partial z}\right)\right]dz,\ K_{ij}^{13}=(-R+A_2)\int_{z_e}^{z_{e+1}}\left[\left(\psi_i^e\right)\left(\psi_j^e\right)\right]dz, \\ K_{ij}^{14}=A_3\int_{z_e}^{z_{e+1}}\left[\left(\psi_i^e\right)\left(\frac{\partial\psi_j^e}{\partial z}\right)\right]dz,\ \ K_{ij}^{15}=-Gr\int_{z_e}^{z_{e+1}}\left(\psi_i^e\right)\left(\psi_j^e\right)dz,\ K_{ij}^{16}=-Gm\int_{z_e}^{z_{e+1}}\left(\psi_i^e\right)\left(\psi_j^e\right)dz, \\ M_{ij}^{11}=\int_{z_e}^{z_{e+1}}\left(\psi_i^e\right)\left(\psi_j^e\right)dz,\ \ M_{ij}^{12}=M_{ij}^{13}=M_{ij}^{14}=M_{ij}^{15}=M_{ij}^{16}=0, \end{cases} \tag{39}$$

$$\begin{cases} K_{ij}^{21}=-S\int_{z_e}^{z_{e+1}}\left[\left(\psi_i^e\right)\left(\frac{\partial\psi_j^e}{\partial z}\right)\right]dz,\ K_{ij}^{22}=A_1\int_{z_e}^{z_{e+1}}\left[\left(\frac{\partial\psi_i^e}{\partial z}\right)\left(\frac{\partial\psi_j^e}{\partial z}\right)\right]dz,\ K_{ij}^{23}=(R+A_2)\int_{z_e}^{z_{e+1}}\left[\left(\psi_i^e\right)\left(\psi_j^e\right)\right]dz, \\ K_{ij}^{24}=A_3\int_{z_e}^{z_{e+1}}\left[\left(\psi_i^e\right)\left(\frac{\partial\psi_j^e}{\partial z}\right)\right]dz,\ \ K_{ij}^{25}=0,\ K_{ij}^{26}=0, \\ M_{ij}^{21}=0,\ M_{ij}^{22}=\int_{z_e}^{z_{e+1}}\left(\psi_i^e\right)\left(\psi_j^e\right)dz, M_{ij}^{23}=M_{ij}^{24}=M_{ij}^{25}=M_{ij}^{26}=0, \end{cases} \tag{40}$$

$$\begin{cases} K_{ij}^{31}=0, K_{ij}^{32}=0, K_{ij}^{33}=-S\int_{z_e}^{z_{e+1}}\left[\left(\psi_i^e\right)\left(\frac{\partial\psi_j^e}{\partial z}\right)\right]dz,\ K_{ij}^{34}=\lambda\int_{z_e}^{z_{e+1}}\left[\left(\frac{\partial\psi_i^e}{\partial z}\right)\left(\frac{\partial\psi_j^e}{\partial z}\right)\right]dz,\ , \\ K_{ij}^{35}=0,\ \ K_{ij}^{36}=0 \\ M_{ij}^{31}=0,\ \ M_{ij}^{32}=M_{ij}^{33}=\int_{z_e}^{z_{e+1}}\left(\psi_i^e\right)\left(\psi_j^e\right)dz, M_{ij}^{34}=M_{ij}^{35}=M_{ij}^{36}=0, \end{cases} \tag{41}$$

$$\begin{cases} K_{ij}^{41}=0, K_{ij}^{42}=0, K_{ij}^{43}=0, K_{ij}^{44}=-S\int_{z_e}^{z_{e+1}}\left[\left(\psi_i^e\right)\left(\frac{\partial\psi_j^e}{\partial z}\right)\right]dz,\ K_{ij}^{45}=\lambda\int_{z_e}^{z_{e+1}}\left[\left(\frac{\partial\psi_i^e}{\partial z}\right)\left(\frac{\partial\psi_j^e}{\partial z}\right)\right]dz,\ , \\ K_{ij}^{46}=0 \\ M_{ij}^{41}=0,\ \ M_{ij}^{42}=M_{ij}^{43}=, M_{ij}^{44}=\int_{z_e}^{z_{e+1}}\left(\psi_i^e\right)\left(\psi_j^e\right)dz,\ M_{ij}^{45}=M_{ij}^{46}=0, \end{cases} \tag{42}$$

$$\begin{cases} K_{ij}^{51}=0,\ K_{ij}^{51}=0,\ \ K_{ij}^{53}=-S\int_{z_e}^{z_{e+1}}\left[\left(\psi_i^e\right)\left(\frac{\partial\psi_j^e}{\partial z}\right)\right]dz,\ K_{ij}^{54}=A_4\int_{z_e}^{z_{e+1}}\left[\left(\frac{\partial\psi_i^e}{\partial z}\right)\left(\frac{\partial\psi_j^e}{\partial z}\right)\right]dz,\ , \\ K_{ij}^{55}=-Ec\int_{z_e}^{z_{e+1}}\left[\left(\psi_i^e\right)\left(\frac{\partial\bar{u}}{\partial z}\right)\left(\frac{\partial\psi_j^e}{\partial z}\right)\right]dz,\ \ K_{ij}^{56}=0, \\ M_{ij}^{51}=0,\ M_{ij}^{52}=0, M_{ij}^{53}=0, M_{ij}^{54}=0, M_{ij}^{55}=\int_{z_e}^{z_{e+1}}\left(\psi_i^e\right)\left(\psi_j^e\right)dz, M_{ij}^{56}=0, \end{cases} \tag{43}$$

$$\begin{cases} K_{ij}^{61}=0, \quad K_{ij}^{62}=0, \quad K_{ij}^{63}=0, \quad K_{ij}^{64}=-S\int_{z_e}^{z_{e+1}}\left[\left(\psi_i^e\right)\left(\dfrac{\partial\psi_j^e}{\partial z}\right)\right]dz, \\ K_{ij}^{65}=\dfrac{1}{Sc}\int_{z_e}^{z_{e+1}}\left[\left(\dfrac{\partial\psi_i^e}{\partial z}\right)\left(\dfrac{\partial\psi_j^e}{\partial z}\right)\right]dz, \quad K_{ij}^{66}=Kr\int_{z_e}^{z_{e+1}}\left[\left(\psi_j^e\right)\left(\psi_j^e\right)\right]dz, \\ M_{ij}^{61}=0,\ M_{ij}^{62}=0, M_{ij}^{63}=0, M_{ij}^{64}=0, M_{ij}^{65}=0, M_{ij}^{66}=\int_{z_e}^{z_{e+1}}\left(\psi_i^e\right)\left(\psi_j^e\right)dz \end{cases} \tag{44}$$

$$\begin{cases} b_i^{1e}=\left[\left(\psi_i^e\right)\left(\dfrac{\partial u}{\partial z}\right)\right]_{z_e}^{z_{e+1}}, \quad b_i^{2e}=\left[\left(\psi_i^e\right)\left(\dfrac{\partial v}{\partial z}\right)\right]_{z_e}^{z_{e+1}}, b_i^{3e}=\left[\left(\psi_i^e\right)\left(\dfrac{\partial \omega_1}{\partial z}\right)\right]_{z_e}^{z_{e+1}} \\ b_i^{4e}=\left[\left(\psi_i^e\right)\left(\dfrac{\partial \omega_2}{\partial z}\right)\right]_{z_e}^{z_{e+1}}, \ b_i^{5e}=\left[A_5\left(\dfrac{\partial \theta}{\partial z}\right)\right]_{z_e}^{z_{e+1}}, \quad b_i^{6e}=\left[\dfrac{\psi_i^e}{Sc}\left(\dfrac{\partial \phi}{\partial z}\right)\right]_{z_e}^{z_{e+1}} \end{cases} \tag{45}$$

In general, to verify that the converged solutions are indeed correct, i.e. to guarantee grid (mesh) independency, a *grid refinement test* is carried out by dividing the whole domain into successively sized grids 81x81, 101x101 and 121x121 in the *z*-axis direction. Furthermore, the finite element code is run for different grid sizes and for a grid size of 101x101 the solutions are observed to achieve mesh independence. Therefore, for all subsequent computations, a grid size of 101 intervals is elected. The iterative process is terminated when the following conditions fulfilled:

$$\sum_{i,j}\left|\xi^{n+1}-\xi^{n}\right|\le 10^{-6} \tag{46}$$

where $\xi=u,v,\omega_1,\omega_2,\theta,\phi$ and n denotes the iterative step. This criterion maintains high accuracy for coupled multi-physical boundary layer equations. Once the key variables are computed, many wall gradient functions may be automatically evaluated.

Skin-friction components (primary and secondary) are obtained as:

$$C_f=\frac{\tau_w^*}{\rho U_r^2}=\frac{\left(Cf_x+Cf_y\right)}{\rho U_r^2} \text{ where } \tau_w^*=\tau_{w_X}^*+i\tau_{w_Y}^* \text{ here}$$

$$\tau_{w_X}^*=\left[(\mu+K)\frac{\partial u^*}{\partial z^*}+K\omega_1^*\right]=\rho U_r^2\left[(1+\Delta)\frac{\partial u}{\partial z}-\frac{\Delta}{2}\frac{\partial v}{\partial z}\right]$$

$$\tau_{w_Y}^*=\left[(\mu+K)\frac{\partial v^*}{\partial z^*}+K\omega_2^*\right]=\rho U_r^2\left[(1+\Delta)\frac{\partial v}{\partial z}+\frac{\Delta}{2}\frac{\partial u}{\partial z}\right]$$

Finally, skin friction components assume the form:

$$Cf=\frac{\left(Cf_x+Cf_y\right)}{\rho U_r^2} \text{ where}$$

$$C_{f_x}=\rho U_r^2\left[(1+\Delta)\frac{\partial u}{\partial z}-\frac{\Delta}{2}\frac{\partial v}{\partial z}\right], \quad C_{f_y}=\rho U_r^2\left[(1+\Delta)\frac{\partial v}{\partial z}+\frac{\Delta}{2}\frac{\partial u}{\partial z}\right] \tag{47}$$

Wall couple stress components (primary and secondary) are computed as:

$$C_w=\left(C_{w_X}+iC_{w_Y}\right) \text{where } C_{w_X}=\left[\frac{\partial \omega_1}{\partial z}\right]_{z=0}, \quad C_{w_Y}=\left[\frac{\partial \omega_2}{\partial z}\right]_{z=0} \tag{48}$$

The plate surface rate of the heat transfer i.e. *Nusselt number* emerges as:

$$Nu = x\frac{\left(\partial T / \partial z\right)}{\left(T_w = T_\infty\right)}\Bigg|_{z^*=0} \Rightarrow Nu\, Re_x^{-1} = -\left[\frac{\partial \theta(0)}{\partial z}\right] \tag{49}$$

The plate surface rate of mass transfer i.e. *Sherwood number* is calculated with:

$$Sh = x\frac{\left(\partial C / \partial z\right)}{\left(C_w = C_\infty\right)}\Bigg|_{z^*=0} \Rightarrow Sh\, Re_x^{-1} = -\left[\frac{\partial \phi(0)}{\partial z}\right] \tag{50}$$

It is important to note that the present simulation extends the conventional studies by including a secondary component for the wall couple stress function. This allows further sophistication in analyzing the micro-element gyration field near the plate surface, a characteristic which is usually only addressed by a single couple stress function as noted by (Gorla, 1988; Eringen, 1976). Furthermore, we note that the micro-rotation boundary conditions in (23) reflect the physically realistic condition – see (Ahmadi, 1976) wherein the wall gradient of the gyration vector must approach zero at the wall. This accommodates the framework of boundary layer growth at the wall, which is violated by the often-simple reduction to a vanishing micro-rotation boundary condition. Micro-element rotary motions will be inhibited at the wall but not eliminated completely. The micropolar theory model's fluids comprising non-deformable micro-elements. The ratio of Eringen micropolar vortex viscosity to Newtonian dynamic viscosity $(\Delta)$and the ratio of gyro-viscosity to Newtonian dynamic viscosity (as encompassed in λ) quantify respectively the relative strengths of the micro-structural coupling to the viscous effect and the couple stress to the viscous effect. They may assume any values greater than or equal to zero. In the vanishing case $\Delta = \lambda = 0$, the elegance of the micropolar model is reflected since the Newtonian (Navier-Stokes) viscous flow case is then extracted. At the opposite end of the spectrum, for $\Delta \to \infty$,the implication is that couple stresses are infinite with respect to the viscous effect. However, this is not physically realizable in industrial fluids and generically intermediate values are studied which provide a good approximation for progressively greater concentrations of micro-elements (Latiff *et al.,* 2016; Thirupathi *et al.,* 2017).

4. GRID SENSITIVITY OF FEM SOLUTIONS

The numerical values of primary and secondary velocities u,v ,primary and secondary angular velocities ω_1,ω_2 , temperature θ and concentration ϕ for different grid sizes are shown in Table 1. From this it reflects the physically realistic results. Hence, this method has been proven to be adequate and gives adequate results for conservation equations.

5. VALIDATION OF FEM SOLUTIONS

The boundary value problem comprising the dimensionless system of equations (17) – (22) subject to (23) are solved with a Galerkin finite element method. Although grid-independence has been achieved, further verification of computations is provided against analytical solutions from the literature, as presented in **Tables 2-4**. **Table 2** presents a comparison between analytical and numerical results for skin friction and couple stress (C_f, C_w i.e. only primary components considered) with variation of 4 key parameters, namely Eringen coupling parameter (Δ), reaction parameter (K_r),rotation parameter (R) and suction parameter (S). It must be mentioned that in the case of *F=Ec=0* (i.e. vanishing radiative flux and zero viscous dissipation) the present results are excellent agreement with the perturbation solutions of (Bakr, 2011). Tables3 and 4 depicts the

comparison between analytical and numerical results for various parameters on primary and secondary shear stress and wall couple stress components (Cf_x, Cf_y, Cw_x, Cw_y). Table 3 considers the case of *Ec= Kr=0*, (i.e. vanishing viscous dissipation, no chemical reaction) and Table 4 considers *Q = Ec= Kr=0*, (i.e. absence of heat source, vanishing viscous dissipation, no chemical reaction). Evidently excellent correlation is achieved in all three tables with the results reported by (Bakr, 2013). It is interesting to note that in Table 2 generally, positive results are obtained for the primary skin friction and wall couple stress. There is no reversal in either linear velocity or micro-rotation field at the wall is computed for any value of the varied parameters.

Conversely in Tables 3, 4, a combination of negative and positive values, are observed for the primary and secondary components of skin friction and wall couple stress. There is therefore significant fluctuation in velocity and micro-rotation fields at the wall when secondary flow is present. This behaviour is not captured in the absence of secondary effects.

6. NUMERICALRESULTS AND DISCUSSION

The evolution of translation velocity components (u, v), microrotation velocity components (gyration fields) (ω_1, ω_2), temperature (θ) and concentration (ϕ) profiles are illustrated in **Figs. 2-31**, for selected parameters i.e. Δ, S, R, F, Q, and Kr. The following default parameter values are implemented in all the finite element computations: $nt = \pi/2, \varepsilon = 0.01$, $n = 10$, $Gr = 10, Gm = 4$, $M = 0.5, K = 5, Sc = 0.6, Pr = 0.7$. We do not explicitly consider oscillatory velocity influence since this has been thoroughly appraised in other studied – see Ganapathy (1994). Weak transverse magnetic field is considered $(M = 0.5)$ and strong thermal and species buoyancy effects. High permeability is examined (when $K \to \infty$ the purely fluid regime is recovered i.e. vanishing porous media fibers, and the Darcian drag components in the primary and secondary momenta eqns. ($-(1/K)u$ and $-(1/K)v$ vanish).

Figs. 2 and 3 depict the impact of micropolar vortex viscosity (coupling) parameter (Δ) on the translational (linear)primary and secondary velocity profiles. With increasing vortex viscosity of micro-elements, the primary velocity u distribution (Fig.2) is significantly enhanced with transverse coordinate (normal to the plate) with maximum acceleration computed a short distance from the plate surface. No cross-over of profiles is observed and positive magnitudes are sustained indicating that backflow never arises. Similarly, with increasing vortex viscosity of micro-elements, the secondary velocity v distribution (Fig.3) is significantly reduced.

Figs. 4 and 5 present the response in angular velocity (micro-rotation) components with coupling parameter (Δ). In contrast to the primary linear velocity field, the primary angular velocity ω_1 decreases with greater vortex viscosity whereas the secondary angular velocity ω_2 increases (again the opposite effect to the secondary linear velocity field). The increasing concentration of micro-elements which enhances vortex viscosity (reflected in higher Δ values) damps the *primary* gyratory motions of micro-elements and the loss in angular momentum in the primary field is transferred to the secondary field where gyration is elevated. The maximum influence is at the wall since with greater concentration of micro-elements, these micro-elements are physically impaired from rotating near the boundary more than anywhere else in the fluid regime. This effect is

progressively reduced with distance from the plate. These computations concur with the earlier observations of (Das, 2011; Gorla *et al.*1988).

Fig. 6 illustrates the variation in temperature profile (θ) for different values of thermal radiation parameter (F) for both Newtonian and micropolar cases. Since the thermal conduction is dominant for large values of F, therefore as F increases the temperature decreases and results in a depletion in thickness of thermal boundary layer. A reduction in radiative flux therefore leads to cooling of the micropolar fluid. Further, it is also observed that fluid temperature is lower for micropolar fluids than for Newtonian fluids. This confirms the cooling characteristics of micro-elements (observed in numerous other studies e.g. Latiff et al., 2016) which may be exploited in materials processing and thermal regulation.

Fig. 7 presents the effect of Eckert number on temperature profiles. *Ec* expresses the relative contribution of kinetic energy in the flow and the enthalpy difference in the boundary layer. It embodies the conversion of kinetic energy into thermal energy by work done against the viscous fluid stresses. Hence temperature is markedly boosted.

Figs. 8-9 depict the distributions of u, v to a variation in thermal Grashof number (Gr) and solutal Grashof number (Gm). Primary translational velocity increases strongly with an increase in both Gr and Gm. Further, the velocity near the wall of the porous plate increases rapidly and the primary velocity overshoot is pushed further from the plate with increasing thermal and species buoyancy effects. Secondary angular velocity is also enhanced with increasing thermal and species Grashof numbers. The positive values of Gr correspond to cooling of the surface by natural convection currents. Similarly, positive Gm implies a reduction in wall mass transfer rate. The enhancement in primary velocity and secondary angular velocity is associated with the body forces, $+Gr\theta + Gm\phi$ and $\Delta\left(\partial\omega_2 / \partial z\right)$ in the primary momentum eqn. (17). This induces a significant acceleration effect directly on u and indirectly on v via the coupling with the secondary angular momentum equation (20). However, buoyancy terms do not feature in either the secondary linear momentum eqn. (18) or the primary angular velocity eqn. (19) and therefore negligible modifications in these components are computed (not shown).

Figs. 10-11 indicate that with increasing magnetic parameter (M) there is a decrease in the primary fluid velocity u and increasing secondary fluid velocity v. The Lorentz magnetic drag force i.e. $-Mu$ in eqn. (17) is generated by the application of magnetic field in the *z*-direction (transverse to the primary velocity direction). This retards the primary flow whereas it accelerates the secondary flow via re-distribution in linear momentum. Significant flow alteration is therefore achieved with even a relatively weak increase in magnetic field. Maximum primary velocity and minimum secondary flow velocity therefore respectively correspond to $M = 0$ (vanishing magnetic field i.e. electrically non-conducting micropolar flow case).

Figs. 12-13 present the influence of magnetic body force parameter (M) on primary angular velocity ω_1 and secondary angular velocity ω_2. The Lorentz drag component $-Mv$ in the secondary linear momentum eqn. (18) as expected induces a marked retardation in primary angular velocity via the coupling term, $+\Delta(\partial\omega_1 / \partial z)$ which indirectly influences the primary angular

velocity field. The secondary angular velocity increases with the increase of M since the term $-\Delta\left(\partial\omega_2/\partial z\right)$couples the secondary angular momentum field to the primary linear momentum field and the drag component, $-Mu$.

Figs. 14-15 present the impact of permeability parameter (K) on both primary and secondary velocites. This parameter characterizes the hydrauic transmissivity of the porous medium. It arises in primary and secondary linear momentum equations (17) and (18), as $-(1/K)u$ *and* $-(1/K)v$ .With increasing permeability, the regime solid fibers progressively decrease. This results in acceleration in the primary translational velocity and deceleration in secondary velocity. This behaviour is sustained across the boundary layer. The presence of a low permeability porous medium therefore damps the primary flow and boosts the secondary flow and vice versa for larger permeability media.

Figs.16-17 depict the response in the angular velocity (micro-rotation) components to variation in permeability parameter (K). The reverse behaviour is observed compared with the linear velocity components. Primary angular velocity is reduced with greater permeability parameter (Fig. 16) i.e. the spin of micro-elements is damped with decreasing porous material fibers. Conversely the secondary angular velocity is accentuated indicating that micro-element spin (gyratory motion) is encouraged with greater permeability.

Figs. 18-21 present the response in u, v, ω_1 and ω_2 profiles for various values of suction parameter S, against spanwise coordinate, z .It is noticed that increasing suction significantly decreases primary linear velocity i.e. decelerates the boundary layer flow. Greater suction corresponds physically to removal of micropolar fluid via the wall. This destroys momentum, and causes the boundary layer to adhere to the wall thereby stabilizing boundary layer growth due to which the primary velocity of the fluid decreases, i.e., the flow is decelerated. However, the opposite behavior is computed for the secondary velocity which is enhanced with greater suction at the plate surface. The case $S < 0$ corresponds to blowing (mass injection) at the wall and is not relevant to the current study and has therefore not been addressed. A similar behaviour is observed in the case of angular velocities i.e. primary angular velocity decreases. With increasing wall suction, primary micro-rotation (ω_1) i.e. gyratory motion (spin) of micro-elements is damped significantly whereas secondary angular velocity is elevated markedly i.e. secondary gyratory motion (spin) of micro-elements $(\omega_2)$is boosted. Further, it is also observed that fluid velocity and angular velocity is consistently lower for micropolar fluids $(\Delta > 0)$than for Newtonian fluids $(\Delta = 0)$.

Figs. 22-23 depict the evolution in temperature $(\theta)$and concentrations (ϕ)profiles with various suction parameter (S)values. Stronger wall suction significantly diminishes both temperature and concentration distribution, although a greater spread in profiles is computed over the same variation in suction parameter for concentration. Both temperature and concentration reduced with enhanced wall suction. Therefore, a smooth convergence of profiles is achieved asymptotically in free stream.

Figs. 24-27 present the variations in primary and secondary components of translational velocity and angular velocity with rotation parameter, R .The results show that primary velocity decreases

as rotation parameter decreases R increases and conversely enhances the secondary velocity. A reverse phenomenon is observed in primary and secondary angular velocities i.e. primary angular velocity increases and secondary angular velocity decreases as R increases. The rotational parameter, R ,features in the so-called "cross flow terms" see (Greenspan, 1968), $-Rv$ in the primary momentum eqn. (17) and $-Ru$ in the secondary momentum eqn. (18). As R increases the centrifugal force increases (faster angular velocity of rotation of the plate, Ω). The centrifugal effect influences each velocity field via the rotational body force term in the other velocity field equation. Although both terms are negative, only primary linear flow is decelerated and the compensation in momentum assists the secondary flow field. The micropolar coupling terms in both linear momenta equations i.e. $(1+\Delta)\left(\partial^2 u/\partial z^2\right)$, $(1+\Delta)\left(\partial^2 v/\partial z^2\right)$ and additionally the angular momentum coupling terms, viz. $-\Delta\left(\partial\omega_2/\partial z\right)$ and $+\Delta\left(\partial\omega_1/\partial z\right)$,enable the rotational body force effect to impart a considerable influence on the micro-rotation field components. The primary spin of micro-elements is effectively accelerated whereas the secondary spin is retarded. Gyration is therefore substantially modified by rotational (centrifugal) body force. A similar observation has been computed for rotating cone micropolar thermal convection by (Gorla and Takhar, 1994) although they only consider a single micro-rotation component in their analysis.

Figure 28 illustrates the evolution in temperature profiles for different values of Prandtl number (*Pr*). The temperature decays quickly for large values of Prandtl number. The no-slip condition requires that the flow velocity at the surface of a solid object (i.e. barrier) is zero and that the fluid temperature is equal to the surface temperature. The thermal boundary layer thickness is similarly the distance from the body at which the temperature is 99% of the temperature found from an inviscid solution. The ratio of the two thicknesses is dictated by the Prandtl number. For Prandtl number of unity, both boundary layers are of the same However when Prandtl number exceeds unity, the thermal boundary layer is thinner than the velocity boundary layer. Generally, higher *Pr* fluids will have relatively low thermal conductivities which will suppress thermal conduction heat transfer *from the wall* and reduce thermal boundary layer thickness, resulting in lower micropolar fluid temperatures in the boundary layer regime. Smaller values of Pr are equivalent to increasing thermal conductivities, and therefore heat is able to diffuse away from the heated plate more rapidly than for higher values of Pr . Hence in the case of smaller Pr the boundary layer is thicker and the rate of heat transfer *to the wall* is reduced. This has important implications in materials processing since by changing the Prandtl number (related to thermophysical properties of the liquid) the heat transfer characteristics can be dramatically modified. Faster cooling is achieved with denser micropolar liquids compared with lighter ones.

Figure 29 depicts the impact of heat absorption (sink) parameter, *Q*, on temperature profiles. Generally, the presence of heat absorption (mimicking for example thermal sink zones in materials processing operations) has the tendency to reduce the fluid temperatures. The effect is most prominent at some distance from the wall (plate surface). The heat sink effect therefore works effectively in cooling the boundary layer regime and decreases thermal boundary layer thickness.

Figs. 30 and 31 show concentration profiles for different values of Schmidt number *Sc* and chemical reaction parameter, *Kr*. Chosen values of Sc are $Sc = 0.22$ (hydrogen), $Sc = 0.3$ (helium), $Sc = 0.6$ (water vapour) and $Sc = 2.62$ (propyl benzene) at 25^0c temperature and one atmosphere pressure. It is inferred that concentration profiles decrease at all locations with

increasing *Sc*, since smaller values of *Sc* are equivalent to increasing chemical molecular diffusivity. *D* quantifies the relative thickness of linear velocity (hydrodynamic) boundary layer and species (concentration) boundary layer. Evidently, *Sc* modifies significantly the concentration distribution throughout the regime. A similar trend is also seen in case of chemical reaction parameter Kr. Owing to consumption of the reactive species, the concentration magnitudes are suppressed rapidly as Kr increases. Thus, the diffusion rates can be tremendously altered by destructive first order homogenous chemical reaction which thins the concentration boundary layer thickness.

6. CONCLUSIONS

In this paper a numerical investigation has been carried out to examine primary and secondary flow in unsteady magnetohydrodynamic (MHD) free convective micropolar heat and mas transfer from a rotating oscillating porous plate in the presence of thermal radiation, heat sink and dissipation effects. The evolution of primary as well secondary translation velocities and microrotation velocity components, temperature and concentration profiles with selected parameters have been visualized and interpreted in detail. Validation of the finite element numerical solutions with several special analytical solution cases has been included. The important findings are summarized as below:

- Primary translational (linear)flow is accelerated with increasing Eringen micropolar vortex viscosity (coupling) parameter, permeability parameter, thermal Grashof and species Grashof number whereas it is damped (decelerated) with increasing magnetic field parameter, wall suction parameter and rotation (centrifugal) parameter.
- Secondary linear flow is accelerated with increasing magnetic field parameter, wall suction parameter and rotation parameter whereas it is decelerated with greater Eringen coupling parameter and permeability parameter.
- Primary angular velocity (gyration component) increases with rotation parameter whereas the converse effect (deceleration) is induced with increasing Eringen coupling parameter, magnetic body force parameter, permeability parameter and wall suction.
- Secondary angular velocity is depressed with increasing rotational parameter whereas it is accelerated with increasing Eringen coupling parameter, magnetic body force parameter, permeability parameter and wall suction.
- The temperature of the micropolar fluid and thermal boundary layer thickness are both decreased with increasing conduction-radiation parameter, wall suction, Prandtl number and heat sink parameter whereas they are enhanced with increasing dissipation parameter (Eckert number).
- Reactive solute concentration and concentration boundary layer thickness is suppressed with increasing wall suction, Schmidt number and first order chemical reaction parameter.

The present finite element code demonstrates excellent convergence and accuracy features for unsteady micropolar multi-physical flows. It is presently being applied to extend the current study to consider alternative radiative transfer models e.g. P1 approximation, and the results of these efforts will be communicated imminently.

REFERENCES

Abbas, Z., Sheikh, M. and Sajid, M., Diffusion of chemically reactive species in stagnation point flow of a micropolar viscoelastic fluid in a porous medium over a stretching/shrinking sheet. *Revista Mexicana de Fısica*., Vol. **62**, pp. 351–361, 2016.

Ahmadi, G., Self-similar solution of incompressible micropolar boundary layer flow over a semi-infinite plate, *Int. J. Eng. Sci.*, Vol. **14, pp.** 639–646, 1976.

Bakr, A.A., Combined heat and mass transfer in magneto-micropolar fluid flow with thermal radiation in a rotating frame of reference, *Int. J. Energy & Tech*., Vol. **5**, no. 10, pp. 1-9, 2013.

Bakr, A.A., Effect of chemical reaction on MHD free convection and mass transfer flow of a micropolar fluid with oscillatory plate velocity and constant heat source in a rotating frame of reference, *Commun. Nonlinear. Sci. Numer. Sim.,* Vol. **16**, pp. 698-719, 2011.

Bég, O.A., Analytical solutions for magnetohydrodynamic oscillatory rotating plate and channel flows in porous media using a fractional Burgers viscoelastic model, *European Physical Journal Plus.,* Vol. **131**, pp. 140-157, 2016.

Bég, O.A., Ghosh, S.K. and Narahari, M., 2010. Mathematical modelling of oscillatory MHD Couette flow in a rotating highly permeable medium permeated by an oblique magnetic field, *Chem. Eng. Commun.,* Vol. **198**, pp. 235-254, 2010.

Bég, O.A., Ghosh, S.K., Ahmed, S. and Bég, T.A., 2012. Mathematical modelling of oscillatory magneto-convection of a couple stress biofluid in an inclined rotating channel, *J. Mechanics in Medicine and Biology.,* Vol. **12**, no. 3, pp. 1250050-1 to 1250050-35.

Bég, O.A., Mabood, F. and Islam, M.N., Homotopy simulation of nonlinear unsteady rotating nanofluid flow from a spinning body, *Int. J. Eng. Math*., Article ID 272079, (15 pages), 2015.

Bég, O.A., Motsa, S.S., Kadir, A., Bég, T.A. and Islam, M.N., Spectral quasilinear numerical simulation of micropolar convective wall plumes in high permeability porous media. *J. Eng. Thermophysics*., Vol. **25**, no. 4, pp. 1–2, 2016.

Bég, O.A., Uddin, M.J., Bég, T. and Gorla, R.S.R., Numerical simulation of self-similar thermal convection from a spinning cone in anisotropic porous medium. *J. Hydrodynamics Series B.,* Vol. **28**, no. 2, pp. 184-194, 2016.

Bhargava, R., Sharma, R. and Bég, O., Oscillatory chemically-reacting free convection heat and mass transfer in a porous medium with Soret and Dufour effects: finite element modeling, *Int. J. Appl. Math. Mech.,* Vol. **5**, no.6, pp. 15-37, 2009.

Bhatti, M.M., Shahid, A., Bég, O. Anwar and Kadir, A., Numerical study of radiative Maxwell viscoelastic magnetized flow from a stretching permeable sheet with the Cattaneo–Christov heat flux model, *Neural Computing and Applications*, 2017. doi:10.1007/s00521-017-2933-8.

Das, K., Effect of chemical reaction and thermal radiation on heat and mass transfer flow of micropolar fluid in a rotating frame of reference, *Int. J. Heat Mass Transfer*., Vol. **54**, pp. 3505-3513, 2011.

Eringen, A.C., *Continuum Physics- Volume IV*, New York: Academic Press, 1976.

Eringen, A.C., *Micro-Continuum Field Theories: II-Fluent Media*, New York: Springer, 2001.

Fiedler, T., Belova, I.V. and Murch, G.E., A Lattice Monte Carlo analysis on coupled *reaction* and mass diffusion, *Comput. Mat. Sci., Vol.* **47**, pp. 826-831, 2010.

Gajjela, N., Jangili, S., Murthy, J.V.R. and Bég, O.A., Mathematical modelling of entropy generation in magnetized micropolar flow between co-rotating cylinders with internal heat generation, *Alexandria Engineering J.,* Vol. **55**, pp. 1969-1982, 2016.

Ganapathy, R., A note on oscillatory Couette flow in a rotating system, *ASME J. Appl. Mech.* Vol. **61**, pp. 208-209, 1994.

Gómez, M.A., Patino, D., Cosemena, R. and Miguez, J.L., CFD simulation of a solar radiation absorber, *Int. J. Heat and Mass Transfer*., Vol. **57**, pp. 231-240, 2013.

Gorla, R.S.R., Combined forced and free convection from a micropolar boundary layer flow on a vertical flat plate, *Int. J. Eng. Sci.,* Vol. **26, pp.** 385–391, 1988.

Gorla, R.S.R., Mixed convection of a micropolar fluid from a rotating cone, *Int. J. Heat and Fluid Flow.*, Vol. **16**, pp. 69-73, 1995.

Gorla, R.S.R., Takhar, H.S., Boundary layer flow of micropolar fluid on rotating axisymmetric surfaces with a concentrated heat source, *Acta Mechanica*., Vol. **105**, pp. 1–10, 1994.

Greenspan, H.P., *The Theory of Rotating Fluids*, New York: Cambridge University Press,1968.

Harish Babu, D. and Satya Narayana, P.V., Influence of variable permeability and radiation absorption on the heat and mass transfer in MHD micropolar flow over a vertical moving porous plate., *ISRN Thermodynamics*., Vol. 2013, Article ID: 953536 (17 pages). http://dx.doi.org/10.115/2013/953536.

Iynger, T.K.V. and Vani, V.G., Oscillatory flow of a micropolar fluid generated by the rotary oscillations of two concentric spheres, *Int. J. Eng. Sci.,* Vol. **42**, pp. 1035-1059, 2004.

Kee, R.J., Coltrin, M.E. and Glarborg, P., *Chemically Reacting Flow*, Wiley, InterScience, 2003.

Kendoush, A.A., Similarity solution for heat convection from a porous rotating disk in a flow field, *ASME J. Heat Transfer*., Vol. **135**, pp. 1885–1886, 2013.

Khonsari, M.M. and Brewe, D.E., Effect of viscous dissipation on the lubricant characteristics of micropolar fluids, *Acta Mechanica*., Vol. **105**, no. 1, pp. 57-68, 1994.

Kim, Y., Lee, J.C., Analytical studies on MHD oscillatory flow of a micropolar fluid over a vertical porous plate, *Surface and Coating Technology*., Vol. **171**, pp. 187-193, 2003.

Kirwan, A.D., Chang, M.S., On the micropolar Ekman problem, *Int. J. Engng. Sci.*, Vol. **14, pp.** 685 -695, 1976.

Latiff, N.A., Uddin, M.J., Bég, O.A. and Ismail, A.I.M., Unsteady forced bio convection slip flow of a micropolar nanofluid from a stretching/ shrinking sheet, *Proc. IMECHE- Part N: J. Nanoengineering and Nanosystems*., Vol. **230**, pp. 177-187, 2016.

Lee, C.T., Mackley, M.R., Stonestreet, P. and Middelburg, A.P.J., Protein refolding in an oscillatory flow reactor, *Biotechnology Letters*., Vol. **23**, pp. 1899-1901, 2001.

Malpica, F., Moreno, N. and Tremante, A., The two-flux model applied to interaction of radiation and natural convection in the laminar boundary layer. *ASME 2003 Heat Transfer Summer Conference*, July 21–23, Las Vegas, Nevada, USA, 2003.

Maqbool, K., Ayesha, S., Idreesa, S. and Anwar

Mishra, S.R. and Bhatti, M.M., Simultaneous effects of chemical reaction and Ohmic heating with heat and mass transfer over a stretching surface: A numerical study, *Chinese Journal of Chemical Engineering*, Vol. 25, pp. 1137-1142, 2017.

Mishra, S.R., Baag, S. and Mohapatra, D.K., Chemical reaction and Soret effects on hydro-magnetic micropolar fluid along a stretching sheet, *Eng. Sci. Tech: International Journal.*, Vol. **19**, pp. 1919-1928, 2016.

Modather, M., Rashad, A.M. and Chamkha, A.J., An analytical study of MHD heat and mass transfer oscillatory flow of a micropolar fluid over a vertical permeable plate in porous medium, *Turkish. J. Eng. Env. Sci.*, Vol. **33**, pp. 245-257, 2009.

Modest, M.F., *Radiation Heat Transfer*, New York: McGraw-Hill, 1992.

Mohamed, M.S., Saied, M., Jon, T. and Omar, L., An enriched finite element model with *q*-refinement for radiative boundary layers in glass cooling, *J. Computational Physics.*, Vol. **258**, pp. 718-737, 2014.

Murthy, J.V.R., Srinivas, J. and Bég, O.A., Entropy generation analysis of radiative heat transfer effects on channel flow of two immiscible couple stress fluids, *J. Brazilian Soc. Mech. Sci. Eng.*, 2017. doi:10.1007/s40430-017-0752-6.

Nazir, A., Hussain, S. and Shafique, M., The rotationally symmetric flow of micropolar fluids in the presence of an infinite rotating disk, *Appl. Math.*, Vol. **6**, pp. 430-439, 2015.

Olajuwon, B.I., Oahimire, J.I., Unsteady free convection heat and mass transfer in an MHD micropolar fluid in the presence of thermo diffusion and thermal radiation, *Int. J. Pure. Appl. Math*., Vol. **84**, pp. 015-037, 2013.

Pai, S.I. and Scaglione, A.P., Unsteady laminar boundary layers on an infinite plate in an optically thick radiating gas, *Applied Scientific Research*., Vol. **22**, pp. 97–112, 1970.

Pal, D. and Talukdar, B., Perturbation technique for unsteady MHD mixed convection periodic flow, heat and mass transfer in micropolar fluid with chemical reaction in the presence of thermal radiation, *Central European J. Phys.*, Vol. **10**, pp. 1150-1167, 2012.

Papautsky, I., Brazzle, J., Ameel, T. and Frazier, A.B., Laminar fluid behavior in microchannel using micropolar fluid theory, *Sensors and Actuators*., Vol. **73**, pp. 101–108, 1999.

Rahman, M.M. and Al-Lawatia, M., Effects of higher order chemical reaction on micropolar fluid flow on a power law permeable stretched sheet with variable concentration in a porous medium, *Can. J. Chem. Eng.*, Vol. **88**, pp. 23–32, 2010.

Ramkissoon, H., Slow steady rotation of an axially symmetric body in a micropolar fluid, *Appl. Sci. Res.*, Vol. **33**, pp. 243–257, 1977.

Rao, S.K.L.L., Ramacharyulu, N.Ch.P. and Rao, B., Slow steady rotation of a sphere in a micro-polar fluid, *Int. J. Eng. Sci.*, Vol. **7**, pp. 905–916, 1969.

Raptis, A., Perdikis, C., Viscoelastic flow by the presence of radiation. *ZAMP*., Vol. **78**, pp. 277-279, 1988.

Reddy, J.N., An Introduction to the Finite Element Method. New York: McGraw-Hill, 1985.

Reis, N., Vicente, A.A., Teixeira, J.A. and Mackley, M.R., Residence times and mixing of a novel continuous oscillatory flow screening reactor, *Chem. Eng. Sci.*, Vol. **59**, pp. 4967-4974, 2004.

Riley, N., The boundary layer on a rotating ellipse, *Z. Angew. Math. Phys.*, Vol. **47**, pp. 306-312, 1996.

Rosa, R.J, *Magnetohydrodynamic Energy Conversion*, USA: Hemisphere Pub. Corp, 1987.

Sastry, V.U.K. and Rao, V.R.M., Micropolar fluid flow due to an oscillating plane subject to rotation, *Acta Mechanica*., Vol. **33**, pp. 45-53, 1979.

Satya Narayana, P.V., Venkateswarlu, B. and Venkataramana, S., Effect of Hall current and radiation absorption on MHD micropolar fluid in a rotating system, *Ain Shams Eng J.*, Vol. 4, pp. 843-854 (2013).

Satya Narayana, P.V., Venkateswarlu, B. and Venkataramana, S., Effect of chemical reaction and thermal radiation on MHD micropolar fluid in rotating frame of reference with constant heat source, *J. Energy, Heat and Mass Transfer*, Vol. 35, no. 3, pp. 197-214 (2013).

Satya Narayana, P.V., Venkateswarlu, B. and Venkataramana, S., Thermal radiation and heat source effects on MHD nanofluid past a vertical plate in a rotating system with porous medium, *Heat Transfer Asian Reaserch.*, Vol. 44, no. 1, pp. 1-19 (2015).

Seth, G.S., Ansari, Md. and Nandkeolyar, R., MHD natural convection flow with radiative heat transfer past an impulsively moving plate with ramped temperature, *Heat and Mass Transfer*., Vol. **47**, no. 5, pp. 551-561, 2011.

Seth, G.S., Nandkeolyar. and Ansari, M.S., Effect of thermal radiation and rotation on unsteady hydromagnetic free convection flow past an impulsively moving vertical plate with ramped temperature in a porous medium, *J. Fluid Mech.,* Vol**. 6**, no. 1, pp. 27-38 (2013).

Shamshuddin, M.D. and Thirupathi, T., Soret and Dufour effects on unsteady MHD free convective flow of micropolar fluid with oscillatory plate velocity considering viscous dissipation effects, Jurnal Teknlogi., Vol. **79**, no. 4, pp. 123-136, 2017.

Shamshuddin, MD., Bég, O., Sunder Ram, M. and Kadir, A., Finite element computation of multi-physical micropolar transport phenomena from an inclined moving plate in porous media, *Indian J. Physics*., 2017. doi:10.1007/s12648-017-1095-y.

Shamshuddin, MD., Siva Reddy, S. and Bég, O.A., Oscillatory dissipative conjugate heat and mass transfer in chemically-reacting micropolar flow with wall couple stress: Finite element numerical study, Part E: Journal of Process Mechanical Engineering, 2017. DOI:10.1177/0954408917743372.

Sohn, H.Y., Chemical reaction engineering in the chemical processing of metals and inorganic materials Part I: Advances in fluid-solid reaction analysis, *Korean J. Chem. Eng*., Vol. **20**, pp. 185-190, 2003.

Swapna, G., Bég, O.A., Kumar, L. and Singh, B., Finite element analysis of radiative mixed convection magneto-micropolar flow in a Darcian porous medium with variable viscosity and convective surface condition, *Heat Transfer-Asian Research*., Vol. **44**, pp. 515-532, 2015.

Thirupathi, T., Bég, O.A. and Kadir, A., Numerical study of heat source/sink effects on dissipative magnetic nanofluid flow from a non-linear inclined stretching/shrinking sheet, Journal of Molecular Liquids, Vol. 232, pp. 159- 173, 2017.

Thirupathi, T., Bég, O.A. and Siva Reddy, S., Finite element computation of magnetohydrodynamic nanofluid convection from an oscillating inclined plate with radiative Flux, heat source and variable temperature effects, Proc. IMechE Part N: J. Nanomaterials, Nanoengineering and Nanosystems, Vol. 231 (4), pp. 179-194, 2017.

Tischer, S., Li, A., Maier, L. and Deutschmann, O., Interactions between reactive flows and reactive surfaces in heterogeneous catalysis and materials synthesis, *1st International Workshop on Near-Wall Reactive Flows Darmstadt/Seeheim-Jungenheim*, Nov.18-19, Germany, 2010.

Tokis, J.N., Free convection and mass transfer effects on the magnetohydrodynamic flows near a moving plate in a rotating medium, *Astro Phys. Space Sci.*, Vol. **44**, no.12, pp. 291-301, 1988.

Türk, Ö., Tezer-Sezgin, M., FEM solution to natural convection flow of a micropolar nanofluid in the presence of a magnetic field, *Meccanica*., Vol. **52**, pp. 889–901, 2017.

Uddin, M.J., Bég, O.A. and Ismail, A.I., Radiative-convective nanofluid flow past a stretching/shrinking sheet with slip effects, *AIAA J. Thermophysics Heat Transfer*., Vol. **29**, no. 3, pp. 513-523, 2015.

Venkateswarlu, B. and Satya Narayana, P.V., Chemical reaction and radiation absorption effects on the flow and heat transfer of a nanofluid in a rotating system, *Appl. Nanoscience*., Vol. 5, pp. 351-360 (2015).

Wei, X., Cheng, L., Zhang, L. and Zeng, Q., Modeling the effects of reactor wall *reaction* on isothermal CVI process of C/SiC composites, *Comput. Mat. Sci., Vol.* **38**, pp. 702-706, 2007.

Zueco, J., Bég, O.A. and Chang, T.B., Network numerical simulation of two-dimensional nonlinear micropolar hydrodynamics in a Darcian porous medium, *Korean J. Chem. Eng.*, Vol. **26**, no. 5, pp. 1226-1234, 2009.

TABLES

Table.1: Numerical values of $u, v, \omega_1, \omega_2, \theta, \phi$ for variations of mesh sizes

Grid Size=0.01					
u	v	ω_1	ω_2	θ	ϕ
1.015	0	-0.55	0.55	1	1
3.692615	-3.777113	-0.344104	0.344104	0.575667	0.418662
5.645103	-5.549523	-0.189119	0.189120	0.292743	0.175343
4.075523	-4.155844	-0.070451	0.070440	0.149121	0.075861
2.606545	-2.630525	-0.035045	0.035045	0.063523	0.033802
1.531605	-1.534532	-0.024623	0.024623	0.030118	0.015111
0.909117	-0.921104	-0.020441	0.020441	0.012606	0.006854
0.559544	-0.557105	-0.008171	0.008171	0.005211	0.002937
0.252822	-0.251117	-0.005125	0.005135	0.002315	0.001311
0.053531	-0.056608	-0.002644	0.002644	0.000917	0.000310
Grid Size=0.001					
1.015	0	-0.55	0.55	1	1
3.692405	-3.776982	-0.343823	0.343823	0.575532	0.418531
5.644923	-5.549453	-0.188902	0.188902	0.292684	0.175264
4.075389	-4.155689	-0.069839	0.069839	0.148898	0.075683
2.606499	-2.630387	-0.034792	0.034792	0.063384	0.033745
1.531485	-1.534412	-0.024565	0.024565	0.029771	0.015003
0.908921	-0.920543	-0.019892	0.019892	0.012580	0.006678
0.559388	-0.557011	-0.007893	0.007893	0.005115	0.002786
0.252764	-0.251002	-0.005041	0.005041	0.002276	0.001188
0.053411	-0.056522	-0.002580	0.002582	0.000874	0.000286
Grid Size=0.001					
1.015	0	-0.55	0.55	1	1
3.692201	-3.776772	-0.343645	0.343645	0.57539	0.418488
5.643745	-5.549309	-0.188792	0.188792	0.292644	0.175198
4.075221	-4.155566	-0.069691	0.069691	0.148093	0.075481
2.606287	-2.630198	-0.034596	0.034596	0.063222	0.033594
1.531299	-1.534229	-0.024387	0.024384	0.029759	0.014987
0.908765	-0.920388	-0.019665	0.019662	0.012564	0.006586
0.559198	-0.556762	-0.007700	0.007700	0.005000	0.002589
0.252666	-0.250000	-0.005000	0.005000	0.002093	0.001000
0.053299	-0.056379	-0.002559	0.002559	0.000868	0.000286

Table 2: Comparison of C_f and C_w when $F=0, Ec=0$

				Analytical results (Bakr, 2011)		Present FEM results	
Δ	K_r	R	S	C_f	C_w	C_f	C_w
0.2	0.01	0.2	1.0	5.661	1.591	5.660881	1.590083
0.4	0.01	0.2	1.0	6.078	1.133	6.078016	1.133432
1.0	0.01	0.2	1.0	7.010	0.631	7.010023	0.631119
0.2	0.5	0.2	1.0	5.634	1.153	5.634002	1.152577
0.2	1.0	0.2	1.0	4.841	0.990	4.842012	0.990091
0.2	0.01	0.4	1.0	3.917	1.274	3.917431	1.273590
0.2	0.01	0.6	1.0	2.607	0.889	2.607218	0.890221
0.2	0.01	0.2	1.5	6.564	3.346	6.564401	3.346333
0.2	0.01	0.2	2.0	6.552	6.533	6.551669	6.533228

Table 3: Comparison of Cf_x, Cf_y, Cw_x, Cw_y for Q, Gr, Gm when $Ec = K_r = 0$

			Analytical results [Bakr, 2013]				Present FEM results			
Q	Gr	Gm	Cf_x	Cf_y	Cw_x	Cw_y	Cf_x	Cf_y	Cw_x	Cw_y
0.5	10	4.0	2.373	-0.11	-0.015	-0.08	2.372902	-0.108910	-0.014881	-0.080013
1.0	10	4.0	2.819	-0.123	-0.017	-0.947	2.820013	-0.123115	-0.017101	-0.946791
0.5	5.0	4.0	0.881	0.078	-0.019	-0.605	0.880901	0.077890	-0.019016	-0.604610
0.5	10	2.0	1.799	0.323	-0.020	-0.706	1.798817	0.322701	-0.020011	-0.706013

Table 4: Comparison of Cf_x, Cf_y, Cw_x, Cw_y for M , κ , Pr , Sc when $Q=0, Ec=0, and \quad Kr=0$

				Analytical results [Bakr, 2013]				Present FEM results			
M	κ	Pr	Sc	Cf_x	Cf_y	Cw_x	Cw_y	Cf_x	Cf_y	Cw_x	Cw_y
0.5	0.5	0.7	0.6	7.716	2.548	-0.047	-1.344	7.715994	2.548210	-0.047012	-1.344231
1.0	0.5	0.7	0.6	6.846	2.086	-0.039	-1.249	6.846032	2.085709	-0.039034	-1.248871
2.0	0.5	0.7	0.6	5.490	1.490	-0.031	-1.102	5.486109	1.490052	-0.030947	-1.102212
0.5	1.0	0.7	0.6	10.25	4.421	-0.079	-1.623	10.250023	4.422301	-0.079231	-1.622651
0.5	2.0	0.7	0.6	12.58	6.95	-0.123	-1.856	12.576051	6.950333	-0.123111	-1.857010
0.5	0.5	1.0	0.6	7.457	2.427	-0.045	-1.315	7.457341	2.426978	-0.045063	-1.315230
0.5	0.5	3.0	0.6	5.939	1.751	-0.037	-1.146	5.941220	1.751132	-0.036690	-1.146220
2.0	0.5	0.7	1.0	5.302	1.424	-0.03	-1.081	5.301765	1.424441	-0.030036	-1.081003

Figure Captions

Figure 1: Geometry and coordinate system for rotating magnetic micropolar transport from an oscillating plate in porous media

Figure 2: Effect of Δ on primary velocity.

Figure 3: Effect of Δ on secondary velocity.

Figure 4: Effect of Δ on primary angular velocity.

Figure 5. Effect of Δ on secondary angular velocity.

Figure 6. Effect of F on Temperature.

Figure 7. Effect of Ec on Temperature.

Figure 8. Effect of Gr &Gm on primary velocity.

Figure 9. Effect of Gr & Gm on secondary angular velocity.

Figure 10. Effect of *M* on primary velocity.

Figure 11. Effect of *M* on secondary velocity.

Figure 12. Effect of M on primary angular velocity.

Figure 13. Effect of M on secondary angular velocity.

Figure 14. Effect of K on primary velocity.

Figure 15. Effect of K on secondary velocity.

Figure 16. Effect of K on primary angular velocity.

Figure 17. Effect of K on secondary angular velocity.

Figure 18. Effect of S on primary velocity.

Figure 19. Effect of S on secondary velocity.

Figure 20. Effect of ***S*** on primary angular velocity.

Fig. 21. Effect of *S*on secondary angular velocity.

Figure 22. Effect of *S* on temperature.

Figure 23. Effect of S on concentration.

Figure 24. Effect of R on primary velocity.

Figure 25. Effect of R on secondary velocity.

Figure 26. Effect of R on primary angular velocity.

Figure 27. Effect of R on secondary angular velocity.

Figure 28. Effect of Pr on temperature.

Figure 29. Effect of Q on temperature.

Figure 30. Effect of Sc on concentration.

Figure 31. Effect of Kr on concentration.

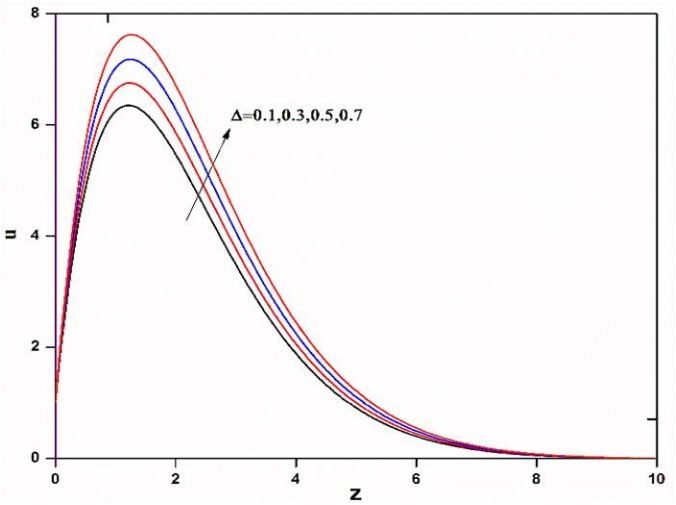

Figure 2. Effect of Δ on primary velocity profiles.

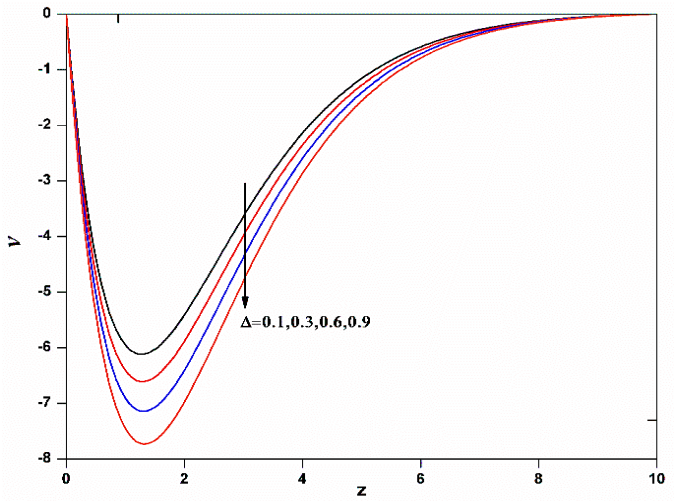

Figure 3. Effect of Δ on secondary velocity profiles.

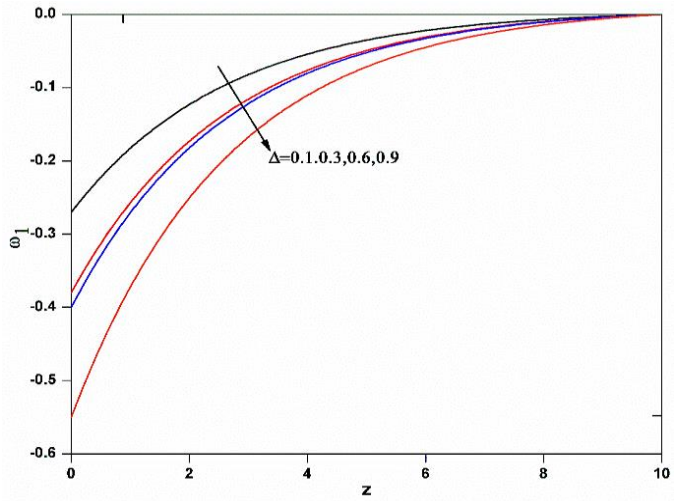

Figure 4. Effect of Δ on primary angular velocity profiles.

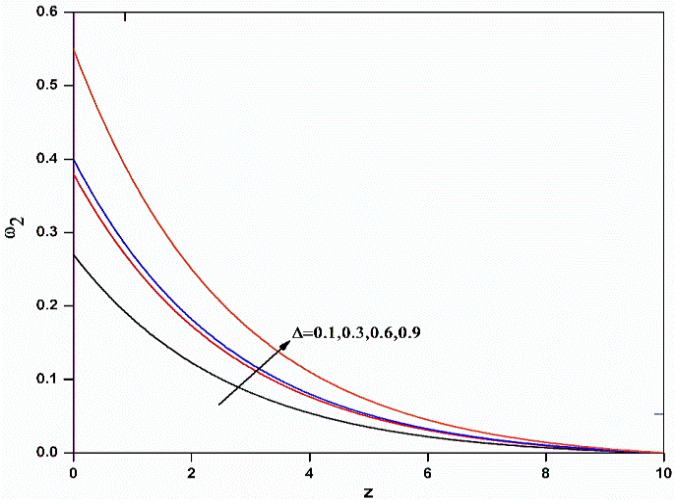

Figure 5. Effect of Δ on secondary angular velocity profiles.

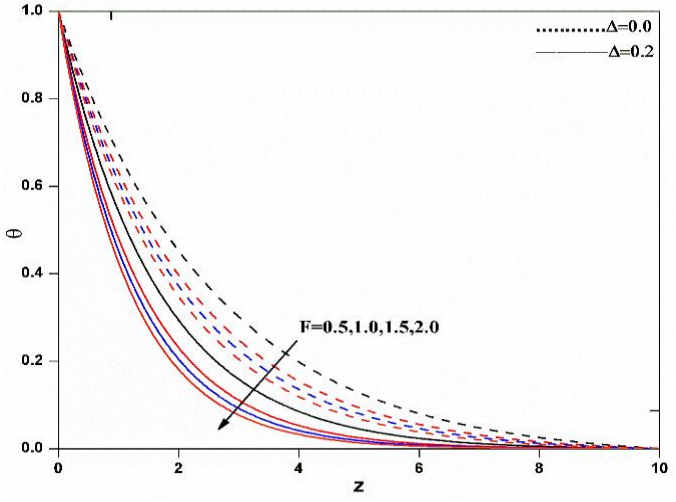

Figure 6. Effect of F on Temperature profiles.

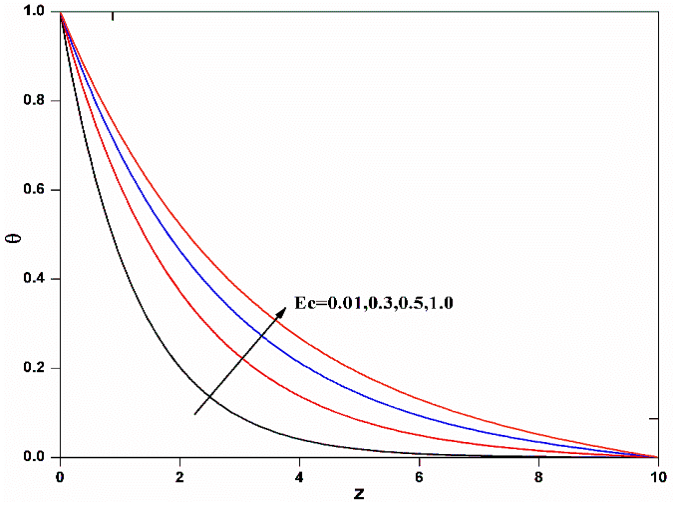

Figure 7. Effect of Ec on Temperature profiles.

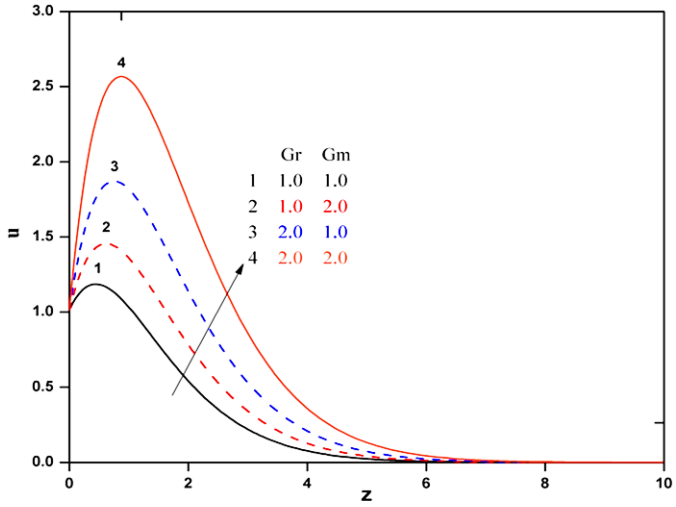

Figure 8. Effect of Gr & Gm on primary velocity profiles.

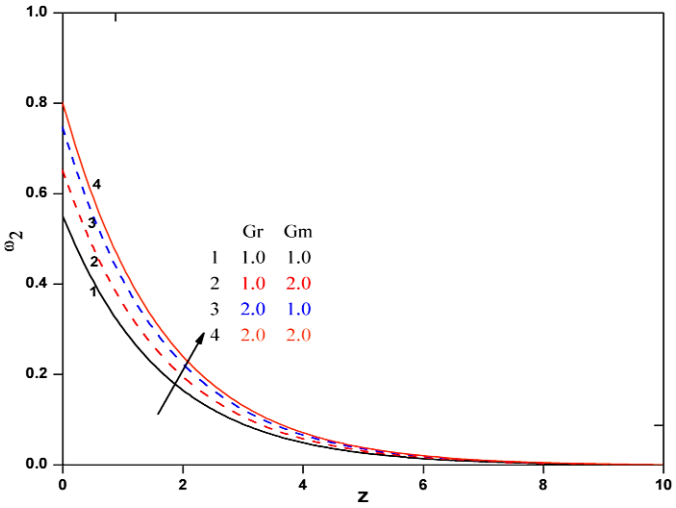

Figure 9. Effect of Gr & Gm on secondary angular velocity profiles.

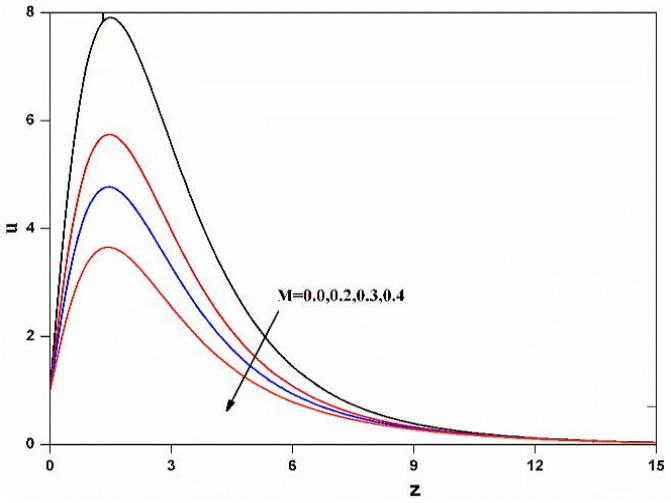

Figure 10. Effect of *M* on primary velocity profiles.

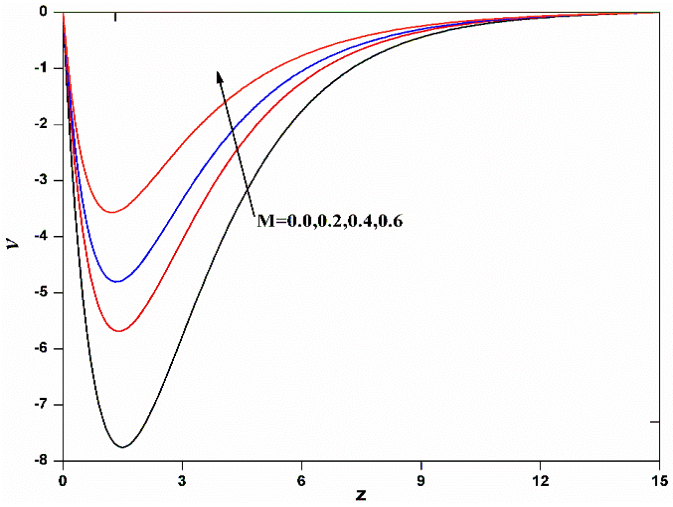

Figure 11. Effect of *M* on secondary velocity profiles.

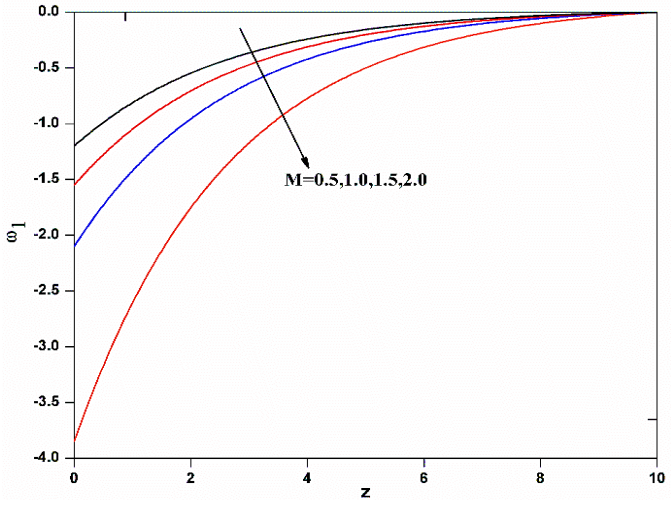

Figure 12. Effect of M on primary angular velocity profiles.

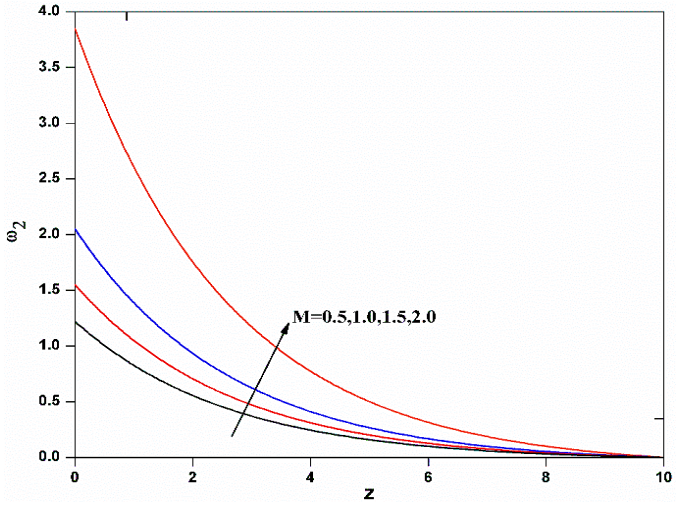

Figure 13. Effect of M on secondary angular velocity profiles.

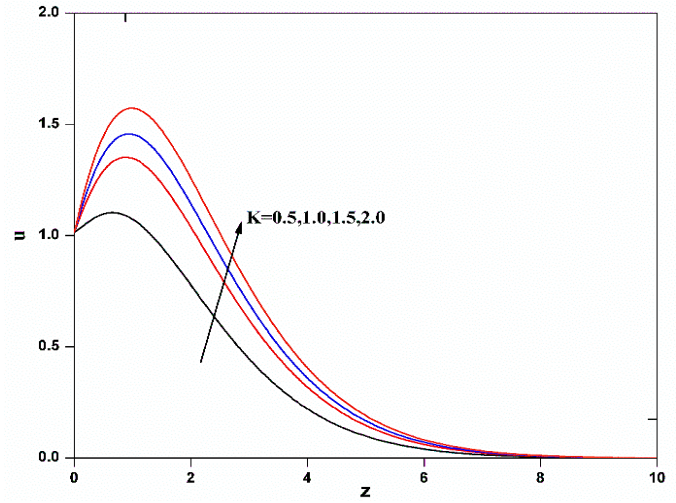

Figure 14. Effect of K on primary velocity profiles.

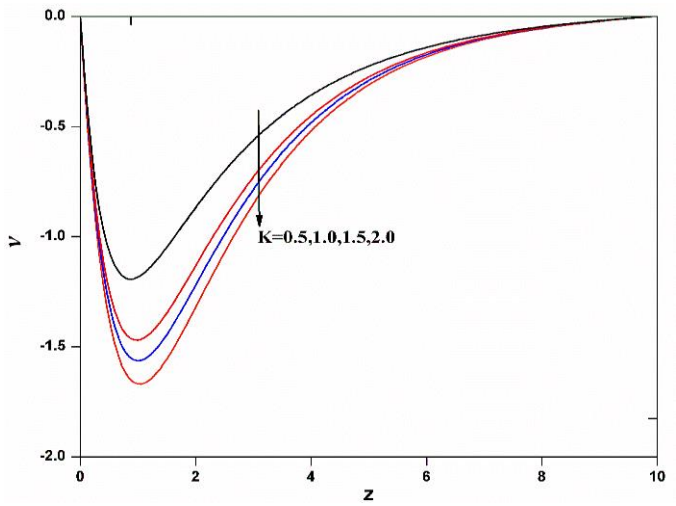

Figure 15. Effect of K on secondary velocity profiles.

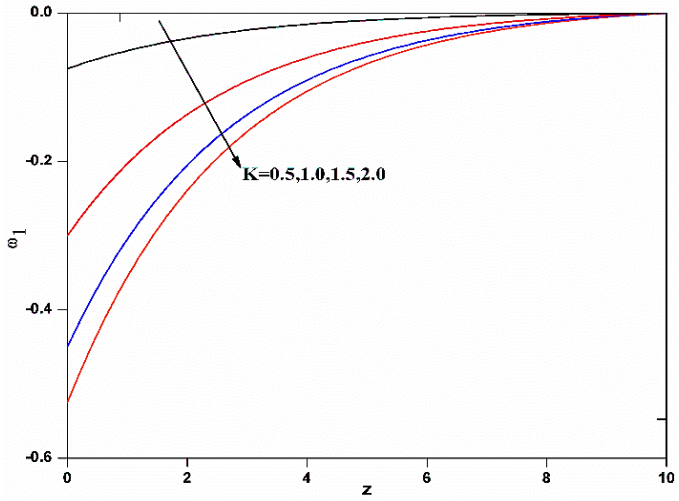

Figure 16. Effect of K on primary angular velocity profiles.

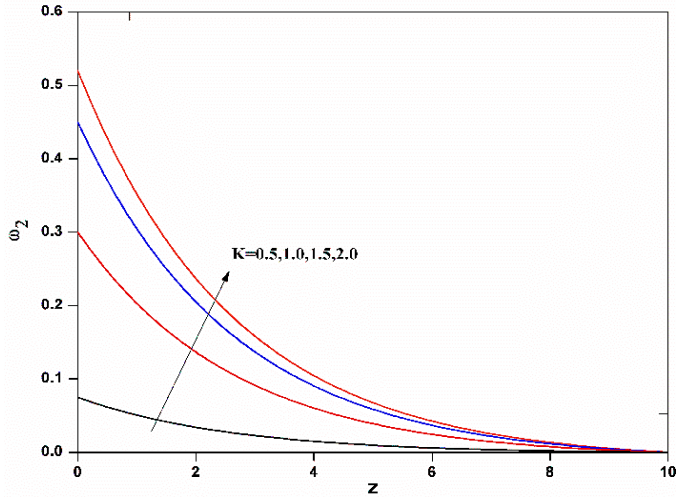

Figure 17. Effect of K on secondary angular velocity profiles.

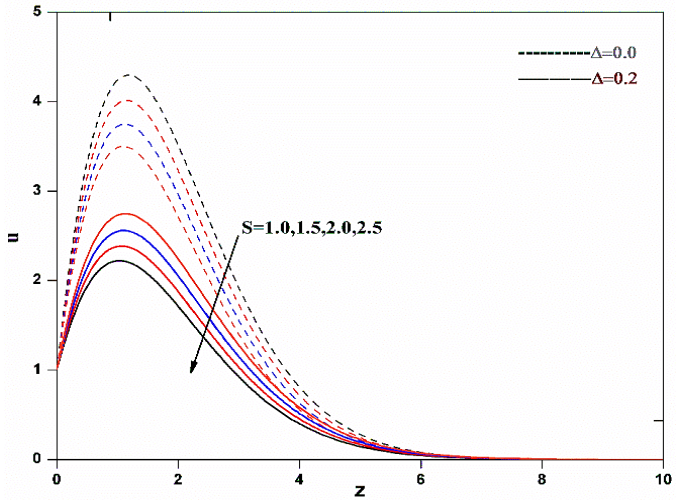

Figure 18. Effect of S on primary velocity profiles.

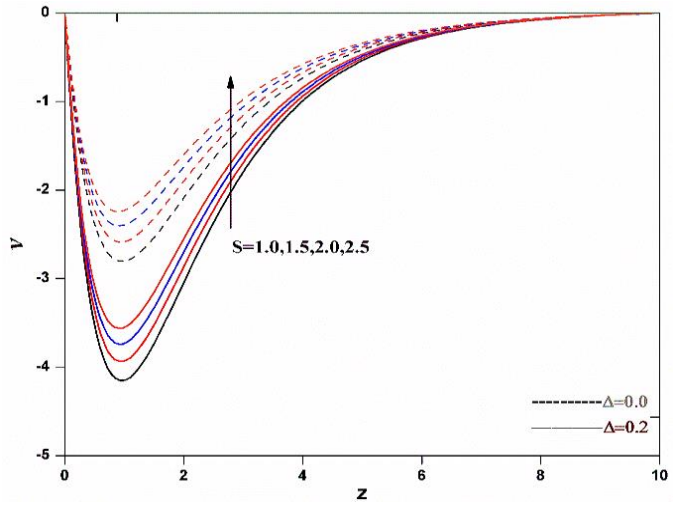

Figure 19. Effect of S on secondary velocity profiles.

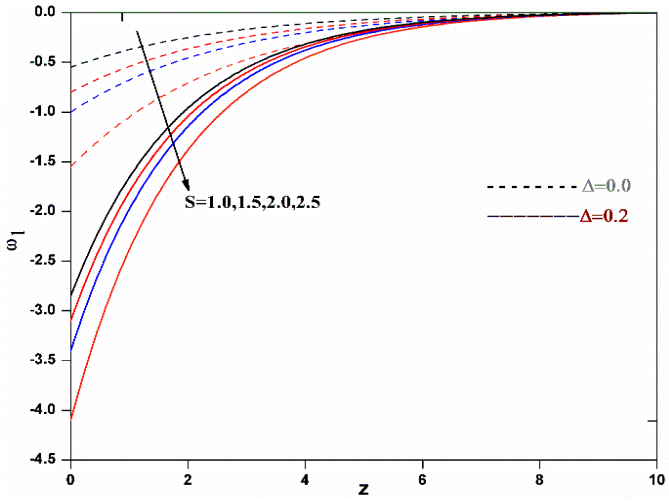

Figure 20. Effect of *S* on primary angular velocity profiles.

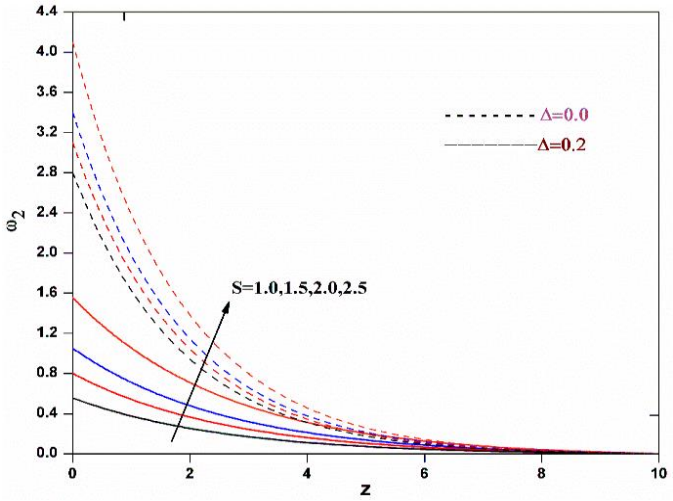

Figure 21. Effect of *S* on secondary angular velocity profiles.

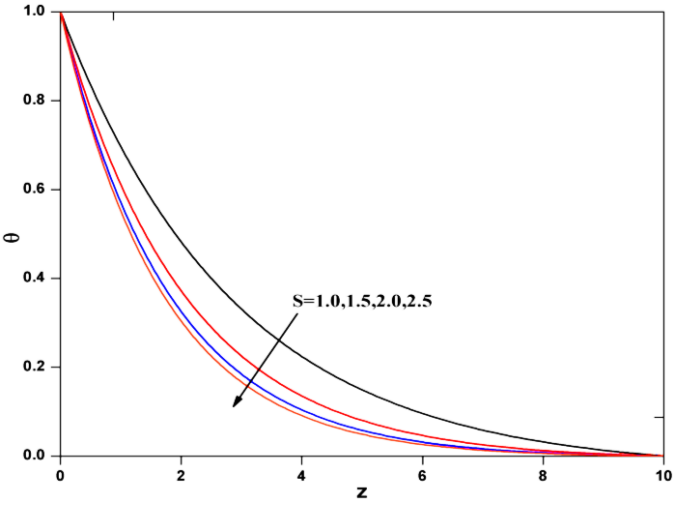

Figure 22. Effect of *S* on temperature profiles.

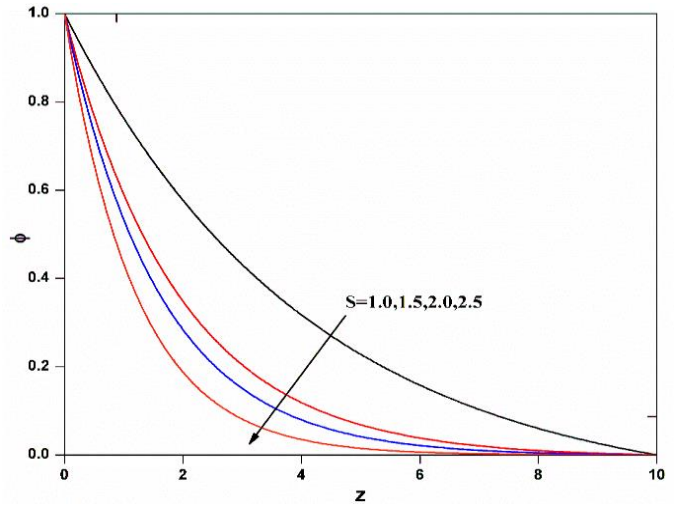

Figure 23. Effect of S on concentration profiles.

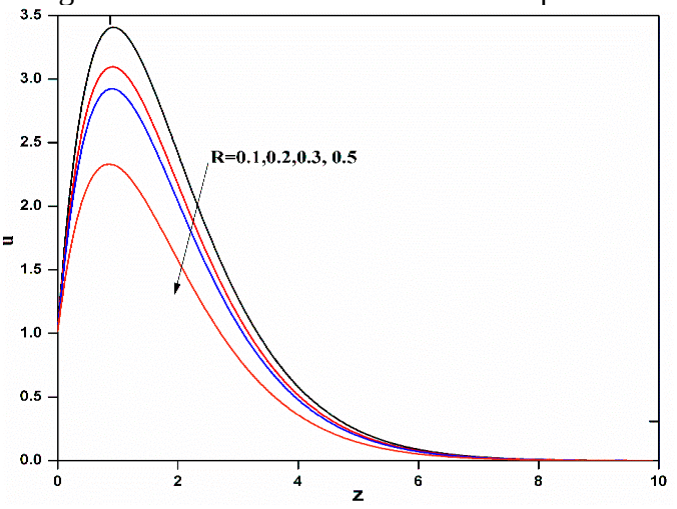

Figure 24. Effect of R on primary velocity profiles.

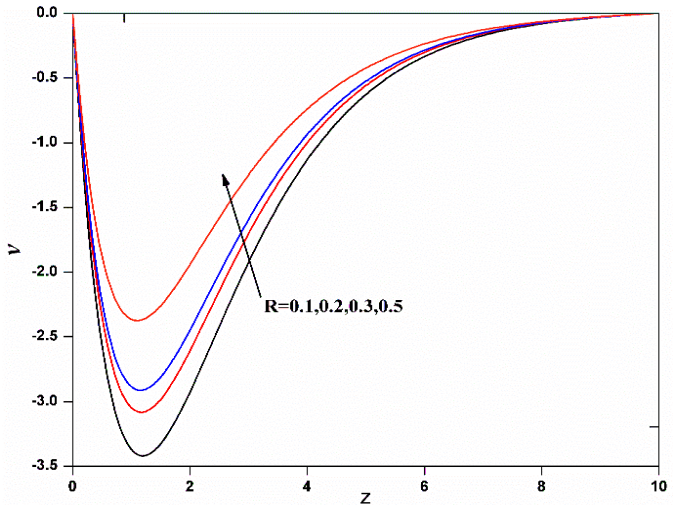

Figure 25. Effect of R on secondary velocity profiles.

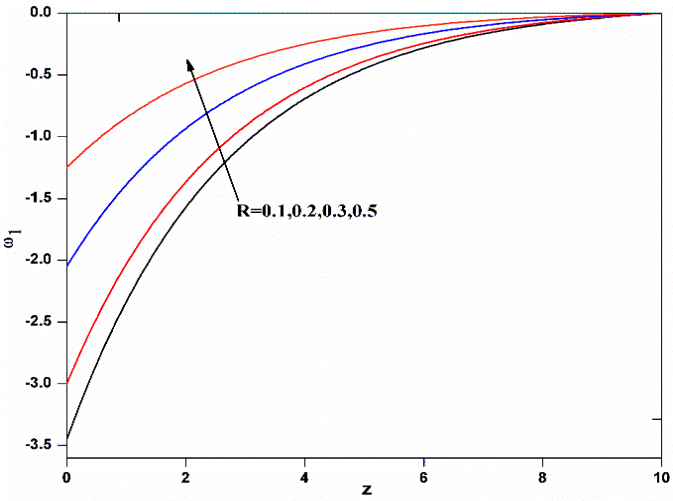

Figure 26. Effect of R on primary angular velocity profiles.

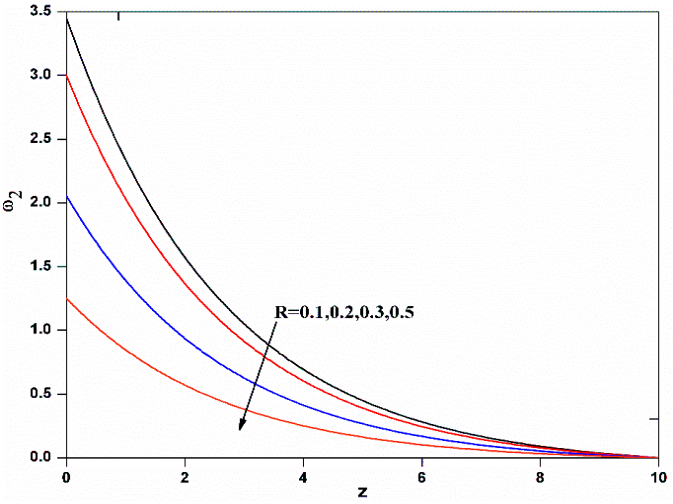

Figure 27. Effect of R on secondary angular velocity profiles.

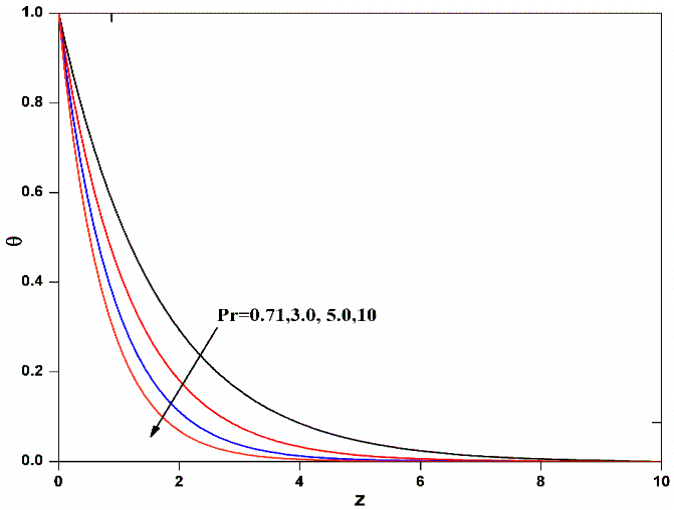

Figure 28. Effect of Pr on temperature profiles.

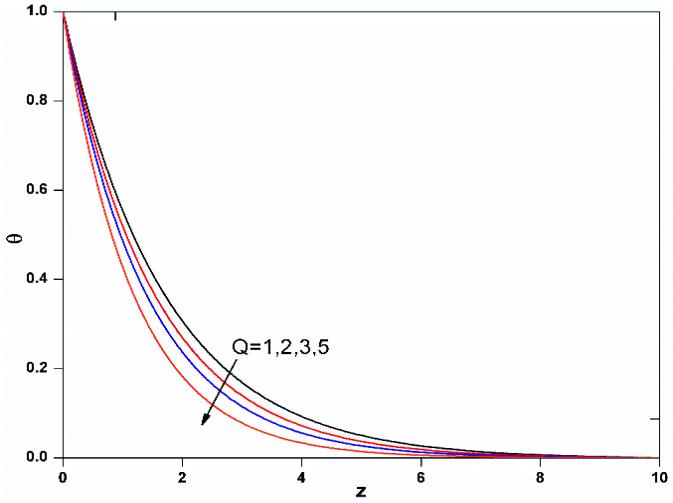

Figure 29. Effect of Q on temperature profiles.

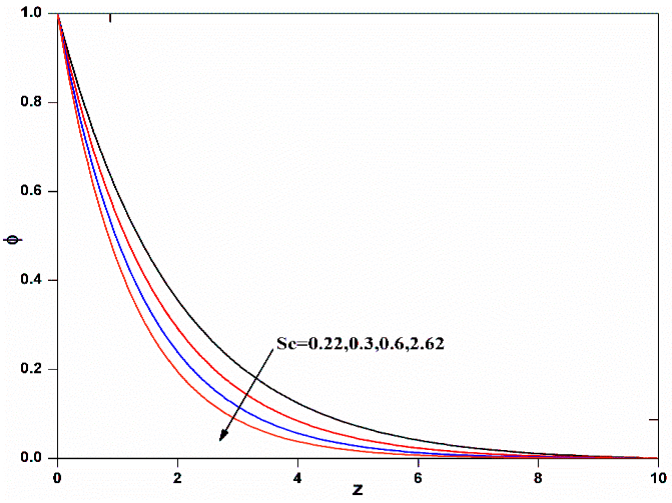

Figure 30. Effect of Sc on concentration profiles.

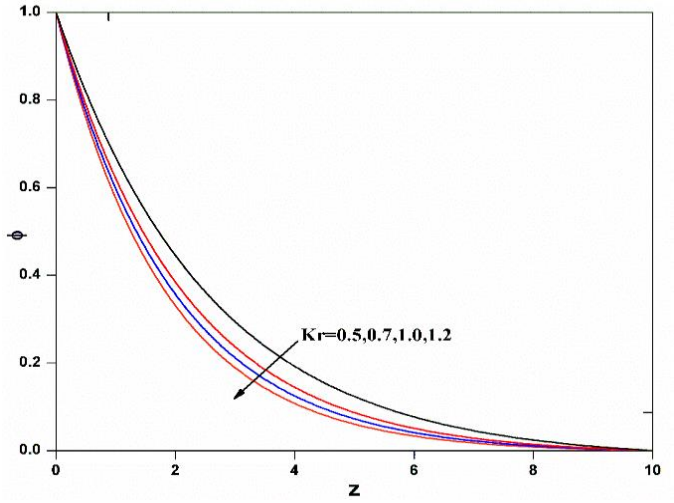

Figure 31. Effect of K_r on concentration profiles.